bioRxiv preprint doi: https://doi.org/10.1101/684464; this version posted June 27, 2019. The copyright holder for this preprint (which was not certified by peer review) is the author/funder. All rights reserved. No reuse allowed without permission.

Multiplexed code of navigation variables in the anterior limbic system

Jean Laurens[1], Amada Abrego[1], Henry Cham[1], Briana Popeney[1], Yan Yu[1], Naama Rotem[1], Janna Aarse[1,2], David Dickman[1,3], Dora Angelaki[1,2]

[1] Department of Neuroscience, Baylor college of Medicine, Houston, Texas, USA.

[2] Center for Neural Science and Tandon School of Engineering, New York University, NY, USA.

[3] Department of Electrical and Computer Engineering, Rice University, Houston, Texas, USA.

Address for correspondence:

Dr. Dora E. Angelaki

Email: da93@nyu.edu

Center for Neural Science, Meyer 901

New York University, NY 10003

Acknowledgements: Supported by the Simons Collaboration on the Global Brain, Grant 542949, by R01 DC004260; and by NIDCD R21 DC015602.

Abstract

The brain's navigation system is a network of brain regions that integrate egocentric sensory information to create a sense of position in allocentric space. Here we used a multimodal model to systematically assess how neurons in several parts of the navigation circuit encode an array of navigational variables. We recorded neuronal activity in the anterior thalamic nuclei, retrosplenial cortex and anterior hippocampus of mice, as well as in the cingulum fiber bundle and the white matter regions surrounding the hippocampus, while animals foraged in a circular arena. As expected, we identified characteristic cell types, such as thalamic head direction cells and hippocampal place and speed cells. In addition, our approach revealed that a population of thalamic cells encode the animal's allocentric position, similar to place cells. We also found that a large fraction of retrosplenial cortex neurons, as well as some hippocampal neurons, encode the egocentric position of the arena's boundary. Neuronal activity in the cingulum fiber bundle, recorded at the level of the anterior retrosplenial cortex, resembled a combination of antero-dorsal thalamus and retrosplenial cortex responses. Fibers travelling through the white matter in the vicinity of the hippocamps carried a mixture of navigation variables. Our results draw a new picture of the signals carried and outputted by the anterior thalamus and retrosplenial cortex, and offer new insights on navigational variables represented in the hippocampus and its vicinity.

bioRxiv preprint doi: https://doi.org/10.1101/684464; this version posted June 27, 2019. The copyright holder for this preprint (which was not certified by peer review) is the author/funder. All rights reserved. No reuse allowed without permission.

Introduction

One of the most striking properties of the rodent navigation system is the existence of characteristic cell populations that represent well-defined navigation variables. For instance, place cells are pyramidal neurons in the hippocampus (O'Keefe 1971, 1796) that encode the animal's allocentric position, and head direction (HD) cells in the antero-dorsal thalamic nuclei form a neuronal compass (Taube et al. 1995; Blair and Sharp 1996; Zugaro et al. 2001; Peyrache et al. 2015,2017; Page et al. 2017). Place cells and HD cells are thought the prominent neuron types in these regions, where no other navigational variables have been reported. In contrast, other regions such as the medial entorhinal cortex (MEC) encode multiple navigation variables and, as revealed by a recent study (Hardcastle et al. 2017), individual neurons often encode multiple variables. May this be a property exclusively for the MEC, or does mixed selectivity represent a generic property throughout the rodent spatial navigation circuit?

Here we used the Linear-Nonlinear (LN) model developed by Hardcastle et al. (2017) to characterize population responses in a network of brain regions involved in navigation. We first recorded neurons in the anterior thalamic nuclei (ATN), and in particular in the antero-dorsal thalamic nuclei, and investigated whether this region may encode spatially modulated variables other than head direction. We also tested whether neuronal firing is phase-locked to theta-band LFP, a property that has never been reported for antero-dorsal thalamus, yet characterizes most spatial navigation regions, including the neighboring antero-ventral thalamic nuclei (Tsanov 2010, 2011). Next, we compared neural selectivity between the ATN and the retrosplenial cortex (RSC), and we noted few similarities. Unlike the ATN, we find that RSC is dominated by the coding of arena boundaries in an egocentric frame of reference (Carstensen et al. 2018; Hinman et al. 2019; see also Peyrache et al. 2017; Wang et al. 2018; Derdikman, 2009). We also characterized neuronal responses in the anterior parts of the hippocampal formation (CA2/CA3). Furthermore, we also used the LN model to re-analyze previously published neuronal data recorded in the ATN and Postsubiculum (Peyrache et al. 2015). Finally, in order to test whether the multiplexed code is communicated among brain areas, we also describe response properties from the cingulum fiber bundle, in the vicinity of Bregma, i.e. at a location where it conveys output fibers from the ATN and RSC (Domesick 1970; van Groen and Vyss 1990,1995, Bubb et al. 2017, 2018).

Results

We used tetrodes bundles to record extracellularly while mice (n=22) foraged in a circular arena (50 cm diameter; 8-minutes recording sessions) (**Fig. 1A**). We sampled 5 different brain regions (**Fig. 1B**): the anterior nuclei of the thalamus (ATN, n=6 animals), which included predominantly of recordings in the antero-dorsal nuclei; the retrosplenial cortex (RSC, n=4 animals); the cingulum fiber bundle (n=7 animals); the anterior portion of the hippocampus (CA2/CA3; n=3 animals); and the white matter region anterior to the hippocampus (Fimbria and fornix; n=6 animals). Multiple regions were sampled sequentially in some animals. Recording locations were verified post-mortem (**Fig. 1C**, see also **Fig. 6-10 S1**). We recorded and analyzed the responses of 1220 neurons (281 in ATN, 180 in RSC, 380 in cingulum, 112 in hippocampus, and 267 in the fimbria).

bioRxiv preprint doi: https://doi.org/10.1101/684464; this version posted June 27, 2019. The copyright holder for this preprint (which was not certified by peer review) is the author/funder. All rights reserved. No reuse allowed without permission.

We used a multivariate linear-nonlinear (LN) model (Hardcastle et al. 2017) to test whether each cell responds significantly to a series of navigational variables (**Fig. 2A**), and to assess whether it is modulated by theta-band (5-12 Hz) LFP. Specifically, we tested the 4 variables considered in (Hardcastle et al. 2017): the animal's allocentric position (AP), head direction (HD) and linear speed (LS) in the environment, as well as the phase of the theta-band LFP rhythm (ΘP), and added two navigational variables: the egocentric position of the arena's boundary relative to the head (EB) and the head's angular speed (AS). The LN model assumes that multiple variables influence the cell's response in a multiplicative manner and uses an optimization procedure to compute each variable's tuning curve to match the recorded firing rate, as shown next. To determine the best model, each cell's response is fitted separately by each model variable alone, or with pairs of variables (or triplets, and so on) and uses a forward search procedure to determine which variables influence the cell's firing significantly (according to the Log-likelihood ratio; see Methods).

Example cells

We first use two well-known neuron types to illustrate the robustness of the model: an example HD cell recorded in the ATN (**Fig. 3**); and an example hippocampal place cell (AP response) that also fired in phase with theta-LFP (ΘP modulation) (**Fig. 4**). Subsequently, we also illustrate examples of a novel cell type in RSC (**Fig. 5**), as well as coding for more multiplexed variables in other cell types.

ATN example cell: The example HD cell fired in intense bursts when the head faced a specific allocentric direction (50°; **Fig. 3A,C**, black). We separated HD in 18 bins and computed the average firing rate within each bin. The resulting tuning curve (**Fig. 3B**) was typical of an ATN HD cell, exhibiting a sharp peak with an average firing of 104 spk/s at the preferred direction. Computing a HD tuning curve in this manner (the 'experimental' tuning curve) is the traditional approach for evaluating HD responses, typically combined with a shuffling-based statistical analysis of the curve's tuning amplitude. By contrast, the LN model fits a tuning curve and uses a cross-validation procedure to test for statistical significance. In this cell, the 'reconstructed' tuning curve (**Fig. 3D**) resembles the experimental tuning curve (**Fig. 3C**).

To evaluate the set of variables encoded by this cell, we first fitted the firing rate based on each of the 6 variables individually (**Fig. 3E**, left). HD provided a considerably better fit, measured by the Log-likelihood ratio, than any other variable, and was selected as the best first-order model. Next, we tested for all 2nd order models by adding one of the 5 remaining variables to HD (**Fig. 3E**, middle). None of these models provided a significant increase in fit quality compared to HD alone. Therefore, the model selection procedure was terminated, and the HD model was selected as the best fitting. The full model including all 6 variables is shown for reference in (**Fig. 3E**, right): it model didn't provide a significantly better fit than the HD model alone.

To quantify tuning strength, we developed a 'normalized tuning amplitude (NTA)', which is equal to the curve's trough to peak amplitude divided by the peak firing rate (itself measured across all tuning curves). For this particular example cell, firing rate varied from practically zero (1 spk/s) to a peak of (104 spk/s), resulting in a NTA of 0.99.

bioRxiv preprint doi: https://doi.org/10.1101/684464; this version posted June 27, 2019. The copyright holder for this preprint (which was not certified by peer review) is the author/funder. All rights reserved. No reuse allowed without permission.

Hippocampal place (AP) cell: Next, we examine an example hippocampal cell that responded to AP and was modulated by ΘP. The model selection process is illustrated in **Fig. 4A**. Across all 1st order models, AP provided the best fit to the data. Next, the process tested all 2nd order models that contained AP and determined that adding ΘP increased the fitting quality significantly. In a next step, none of the 3rd order models that included AP and ΘP provided a significantly better fit than the AP+ΘP model, which was therefore selected as a best-fitting model.

The cell's AP and ΘP response properties are summarized in **Fig. 4B,C**. When the animal explored its environment randomly, neuronal firing occurred preferentially in the lower right portion of the arena (**Fig. 4B**, left). An AP tuning curve, computed by following the usual approach of binning neuronal spiking, exhibited a place field at the corresponding position (**Fig. 4B**, middle). The fitted tuning curve constructed by the LN model resembled the experimental curve (**Fig. 4B**, left; note that is it smoother due to the LN model's smoothness constraint; see Methods). The cell's firing decreased from a peak 10 spk/s to a minimum of 1 spk/s, and accordingly the curve's NTA was 0.9. The cell was phase-locked with the LFP, as shown by the fitted ΘP tuning curve (**Fig. 4C**) with a NTA of 0.57. The simulated firing rate (**Fig. 4D**, red), computed based on the AP and ΘP tuning curve, followed the cell's measured firing well (**Fig. 4D**, black).

Egocentric boundary cell in RSC: The LN model incorporated a variable defined as the egocentric position of the arena's boundary (EB). Because the arena used in the present experiments is circular, knowing the egocentric location of the entire boundary is equivalent to knowing the egocentric location of its closest point (**Fig. 5A,B**), which may be positioned anywhere within 25 cm of the head (**Fig. 5B**; see **Fig. 5S1** for details). How the LN model fits the responses of an example RSC cell with EB tuning is shown in **Fig. 5C,D** (see also **Suppl. Movie 1**). This cell was largely multimodal (**Fig. 5C**): its firing rate (**Fig. 5D**) was affected significantly by head direction and linear as well as angular speed (HD, EB, LS, **Fig. 5E**), in addition to EB (**Fig. 5F**). Nevertheless, the EB response was by far the most predominant (NTA=0.96 versus NTA<=0.17 for all other significant variables).

The preferred EB response occurred in close proximity to the arena's boundary *while* facing directly towards it, i.e. when the boundary was directly in front of the head (**Fig. 5F**, left; **Suppl. Movie 1**). In contrast, the cell was virtually silent when the animal faced away from the boundary, even when it was in close proximity (**Fig. 5F**, left; **Suppl. Movie 1**). Furthermore, the firing was independent of the animal's allocentric location, i.e. the cell could fire anywhere along the boundary, as long as the animal was facing it. Both the experimental and fitted tuning curves exhibited a sharp peak at the corresponding location (**Fig. 5F**, middle and right panels). Note that, due to its EB tuning, the cell fired more on average when the animal's allocentric position (AP) was close to the arena's boundary (**Fig. 5G**). This is apparent on the *experimental* AP tuning curve, which is computed directly from experimental data (**Fig. 5G, middle**). Nevertheless, the model revealed that the cell was not sensitive to allocentric position, and the *fitted* AP tuning curve was flat.

Overview of population responses

Anterior thalamic nuclei

bioRxiv preprint doi: https://doi.org/10.1101/684464; this version posted June 27, 2019. The copyright holder for this preprint (which was not certified by peer review) is the author/funder. All rights reserved. No reuse allowed without permission.

We targeted the antero-dorsal nuclei of the thalamus in 6 animals (**Fig. 6**). Histological localization of the electrode tracks (**Fig. 6S1A**) confirmed that most recordings sites were indeed located in these nuclei. Yet, we can't exclude that some tetrodes may have contacted neighboring nuclei (e.g. antero-ventral or latero-dorsal). Therefore, we refer to these recorded regions as anterior thalamic nuclei (ATN). The proportions of cells characterized as predominantly APC, EBC, HDC, LSC and ASC are shown in **Fig. 6A**. Non-spatially modulated cells are represented by the white area of the chart, and the population of ΘP-modulated cells is outlined in black in each sector. The proportions of cells significantly modulated by any one of the 7 variables are shown as a histogram in **Fig. 6B**. Each bar is broken down into colored segments that represent the predominant variable (e.g., the variable with the highest NTA). Population responses recorded in individual animals are shown in **Fig. 6S1**.

As expected, we found that approximately half (48%) - of ATN cells are HDC, that is, HD is the variable that modulates the cell's firing rate the strongest (**Fig. 6A**). A small fraction of cells exhibited stronger selectivity to another variable, typically AP (12%), EB (5%) or LS (4%) (**Fig. 6A,B**, green, blue and yellow bars). Across the population, the total fraction of HD-tuned ATN cells was 54% (**Fig. 6B**). HD responses typically had very high NTA (**Fig. 6C**, orange; median across all cells with significant HD tuning = 0.87, 1st-9th deciles: 0.47-0.98).

The peak firing rate of HDC varied widely (1st-9th decile: 6-85 spk/s; median: 20 spk/s; **Fig. 6D**). In particular, a large cluster of HDC located in the upper right corner of **Fig. 6D** exhibited vigorous and specific firing (peak >30 spikes/s; NTA≈1), which is generally associated with "typical" HDC. Nevertheless, we also encountered a number of ATN HDC with lower peak responses.

The second spatial variable represented in the ATN was allocentric position; 19% of ATN cells had significant AP responses; **Fig. 6B**), and NTA could reach high values (median = 0.62, 1st-9th deciles: 0.26-0.87, **Fig. 6C**, see example cells in **Fig. 6S2**). A smaller proportion (10%) of ATN cells encoded egocentric boundary (**Fig. 6B**), with substantial NTA (median = 0.58; **Fig. 6C**), and 5% were classified as EBC (**Fig. 6A**). A small proportion (9%) of ATN cells were tuned to linear speed, and 4% were identified as LSC (**Fig. 6A,B**, orange). Nevertheless, linear speed responsiveness was modest (median NTA=0.22; **Fig. 6C**). Angular speed responsiveness was rare (6%) in ATN, and only 2 cells (<1%) were predominantly tuned to AS (**Fig. 6A-C**, violet).

Although it has never before been reported, about half (48%) of ATN cells were modulated by ΘP. Theta phase modulation was most prominent among APC, EBC and LSC (81%), compared to HDC (53%) (**Fig. 6A**). Despite the presence of a theta rhythm in all animals (**Fig. 6S1**), there was a marked inter-animal variability in the fraction of ΘP-modulated HDC: almost all recorded cells in animals H51 and H54, but almost none in animals H71M, H72M and I10M3.

APC and EBC exhibited comparable range of firing as HDC: APC: median = 18 spk/s, 1st-9th deciles: 5-54; EBC: median = 15 spk/s, 1st-9th deciles: 6-56. Thus, in summary, the 3 main classes of spatially tuned ATN neurons (HDC, APC and EBC) could exhibit specific responses (e.g. NTA>0.6; **Fig. 6D**) with occasionally vigorous peak responses (e.g. close to 100 spk/s, **Fig. 6D**), although lower peak responses could also be encountered (e.g. <10spk/s, **Fig. 6D**).

bioRxiv preprint doi: https://doi.org/10.1101/684464; this version posted June 27, 2019. The copyright holder for this preprint (which was not certified by peer review) is the author/funder. All rights reserved. No reuse allowed without permission.

We also quantified additional response parameters. The neuronal firing properties (mean firing rate, CV2 and spike duration) of ATN neurons were broadly distributed (**Fig. 6E,F**): average firing rate ranged from 1.7 to 27 spk/s (1st-9th decile; median=7 spk/s) and CV2 from 0.69 to 1.27 (1st-9th decile; median 0.97). Firing rate and CV2 were inversely correlated (**Fig. 6E;** Spearman rank correlation=-0.75, $p<10^{-10}$). The trough to peak duration of action potentials followed a bimodal distribution (**Fig. 6F**), thus neurons could be separated in clearly distinct groups of short-duration (trough to peak <=0.33ms, 49%) and long-duration (trough to peak >0.33ms, 51%) spikes. Neurons with short and long spike duration had similar mean firing rate (7.2 vs 6.6 spk/s, p=0.13, Wilcoxon rank test) and slightly different CV2 (0.93 vs 1.02, $p=10^{-4}$). A further examination (**Fig. 6S1**) revealed inter-subject differences in firing properties: cells in animals H51M, H54M and H59M were generally low-firing and more irregular and were distributed between short and long-duration spikes, whether cells in animals H71M, H72M and I10M3 had higher firing rates, were more regular and had predominantly low spike duration.

Note that we could not identify any differences in variable coding among narrow and broad spiking neurons. HD cells could exhibit short or long-duration spikes (short- vs long-duration: 85 vs 50 cells, i.e. 63% vs 37%). The two groups exhibited similar mean firing rate (median: 7.8 vs 9.4 spk/s, p=0.6, rank sum test; **Fig. 6E**) and CV2 (0.92 vs 0.99, p=0.07). However, HDC with short-duration spikes had larger NTA (median = 0.92 vs 0.81, $p=3.10^{-5}$, rank sum test) although similar peak firing (23 vs 17 spk/s, p=0.3). We also tested whether narrow and broad spiking neurons were most likely to be ΘP-modulated. To avoid a confounding factor due to inter-animal variability (where neurons H71M, H72M and I10M3 are rarely ΘP-modulated and generally narrow-spiking), we limited this analysis to H51M, H54M and H59M, and excluded non-spatially modulated neurons. We found that narrow and broad spiking neurons were equally likely to be ΘP-modulated (Chi-Square test, $\chi^2=0.073$, n= 1 d.o.f, p=0.78).

Additional ATN recordings (Peyrache et al. 2015)

In order to corroborate our finding that populations of neurons in the ATN encode AP, we analyzed previous recordings published in Peyrache et al. 2015 (**Fig. 6S3,4**). Population responses (**Fig. 6S3**) were similar as in our recordings, and in particular we found substantial fractions of APC in 2 out of 6 animals (**Fig. 6S4**). Peyrache et al. (2015) used probe arrays (8 shanks, 200 µm spacing), which allowed us to investigate the spatial distribution of APC and HDC (**Fig. 6S4**). We found that APC tend to be distributed more laterally than HDC, although the two populations overlap (**Fig. 6S4C**). Furthermore, HDC and APC cells recorded in Peyrache et al. 2015 generally cover three probe shanks (**Fig. 6S4A,B**), which span 400 µm laterally. Since the extent of the antero-dorsal nuclei is at most 400 µm, it is unlikely that all 3 shanks were in this nucleus; and the most lateral of the 3 shanks may have been in an adjacent nucleus (antero-ventral or latero-dorsal). In our study, recordings that identified APC in the ATN were restricted to a single track (since we used one tetrode bundle) and a narrow range of depth (**Fig. 6S4I-K**), and histology indicated that tetrode tracks were located in the antero-dorsal nuclei (**Fig. 6S2A**). Collectively these results suggest that APC exist in at least some portions of the antero-dorsal nuclei, although they may be more numerous in the adjacent antero-ventral or latero-dorsal nuclei.

Retrosplenial cortex

bioRxiv preprint doi: https://doi.org/10.1101/684464; this version posted June 27, 2019. The copyright holder for this preprint (which was not certified by peer review) is the author/funder. All rights reserved. No reuse allowed without permission.

We implanted four animals for recording in the RSC (**Fig. 7**). One implantation (animal AA2) reached the granular cortex, where 119/180 neurons were recorded (**Fig. 7**). The other implantations (animal AA1, AA18, AA20) reached the dysgranular cortex. Responses from these regions were similar (**Fig. 7S1**), thus pooled in **Fig. 7**.

By far, the variable represented in RSC the most was egocentric boundary. About half (45%) of RSC cells were classified as EBC. EB responses exhibited large NTA (median = 0.7; 1st-9th decile: 0.53-0.88; **Fig. 7A-C**; an example EBC is shown in **Fig. 5** and **Suppl. Movie 1**). Peak firing rates (**Fig. 7D**) were clustered around a median value of 7 spk/s (1st-9th decile: 17-48). We found that the 'preferred boundary position' of EBC (i.e. the egocentric boundary position at which their firing was maximal **Fig. 7S2A**) is generally located close to the head (median = 4.95 cm, CI = [4.03-5.8]; **Fig. 7S2B**). In contrast, the egocentric bearing was distributed uniformly (**Fig. 7S2C**), indicating that EBC could respond when the boundary was in front of the head (**Fig. 7S2A,C**: Front; F), to the right, left (R/L in **Fig. 7S2C**), or behind the head (**Fig. 7S2A,C:** Behind; B).

A sizeable fraction of EBC (52%) were significantly tuned to HD (**Fig. 7B**; blue portion of the bar 'HD'), but with modest NTA (median = 0.27, 1st-9th decile: 0.13-0.41; **Fig. 7B**). Likewise, 22% of EBC were tuned to AS (median NTA = 0.27; 1st-9th decile: 0.14-0.48) and 15% were tuned to LS (median NTA = 0.25; 1st-9th decile: 0.08-0.5). This indicates that EBC were often multimodal. It is striking that the majority of cells that exhibited significant HD tuning were in fact EBC.

Beyond EBC, only small fractions of responsive cells were encountered. Only 4% of the population was classified as HDC (**Fig. 7A**), although, as mentioned above, many EBC exhibited significant HD responses. Interestingly, a few (n=5, 3%) ASC were identified, and these cells had large NTA (higher than 0.8 in 4 cells; **Fig. 7D**, magenta). LFP recorded in the RSC exhibited a clear theta rhythm (**Fig. 7S1**). Yet, ΘP responses were practically non-existent.

In general, RSC cells fired in a homogenous and tightly clustered fashion (**Fig. 7E**): the average firing rate was distributed around a median of 8.3 spk/s and ranged from 2.7 to 26 spk/s (1st-9th decile). The CV2 was distributed around a median of 0.84 and ranged from 0.65 to 0.98. Most neurons (145/180, 81%) had long-duration spikes (**Fig. 7F**).

Cingulum fiber bundle

We recorded neuronal activity from the cingulum bundle (**Fig. 7S3,4**). Most recordings (all animals except AA0; **Fig. 7S4**) were located near Bregma, i.e. at the level of the transition between cingular and retrosplenial cortex along the antero-posterior axis. At this level, the cingulum conveys projections from the anterior thalamus and RSC. Therefore, we hypothesized that we would record a majority of units with short-duration spikes, consistent with axonal spikes (Barry 2015), whose firing and response properties resembled a mixture of ATN and RSC neurons. In agreement with this hypothesis, 23% of cells were classified as HDC (**Fig. 7S3A,B**) and 18% as EBC (**Fig. 7S3A,B**). As expected, the majority of neurons (300/380, 79%) had short-duration spikes (**Fig. 7S3F**). These results show that tetrode recording from the cingulum fibers bundles are possible (and, in fact, remarkably easy); and that the section of cingulum we recorded likely conveys fibers projecting from the ATN and RSC.

bioRxiv preprint doi: https://doi.org/10.1101/684464; this version posted June 27, 2019. The copyright holder for this preprint (which was not certified by peer review) is the author/funder. All rights reserved. No reuse allowed without permission.

Postsubiculum

We also analyzed previously published data recorded by Peyrache et al. (2015) in the postsubiculum of three mice (**Fig. 7S5**). We found a large fraction (31%) of HDC (**Fig. 7S5A**), with low or moderate firing rates (**Fig. 7S5D,E**) and long spike duration (**Fig. 7S5F**), consistent with layer 3 pyramidal neurons (Tukker et al. 2015, Preston-Ferrer et al. 2016, Simonnet et al, 2017; Simonnet et Fricker, 2017). The second most prominent population were APC (14%).

Classification of HDC: comparison with other techniques

To better appreciate how the LN model compares to classification methods used in previous studies, we evaluated HD tuning in ATN, RSC and cingulum using conventional approaches (**Fig. 7S6**), which classify cells as HD-tuned if the mean vector length |R| of their experimental HD tuning curve pass a shuffling test or an arbitrary threshold (e.g. 0.26, Jacob et al. 2017, or 0.4, Yoder et al. 2009; Kornienko et al. 2018). We found that strongly tuned HD cells that pass a threshold of |R|>=0.26 are equally well detected by the LN test and other methods. We also found that a shuffling test is more sensitive than the LN model for detecting cells with moderate HD tuning (**Fig. 7S6B**). However, AP or EB tuning can be erroneously interpreted as HD tuning due to sampling non-uniformity (Muller et al. 1994; Cacucci et al. 2004 ; Rubin et al. 2014; **Fig 7S6C**). The LN model is robust to this issue by construction, and a threshold of |R|>0.26 is high enough to rule out such cells. In contrast, using a shuffling test without accounting for AP or EB tuning may produce a moderate number of false positives, which we estimated to be 5-10% of the cells in the regions considered (**Fig. 7S6G-I**). As a conclusion, the LN model is a robust technique for classifying HD cells (as well as other cell types) that agrees well with |R| tests, although it is less sensitive than shuffling tests for cells with low tuning strength.

Hippocampus

Many studies have focused on pyramidal place cells that are identified based on their long spike duration and typically exhibit AP responses. Here we recorded and classified the responses of a variety of cell types, including cells with short- and long-duration spikes, located mainly in the anterior part of the hippocampus.

AP (place) cells: A fifth (19%) of hippocampal cells were classified as APC (**Fig. 8A,B**). A significantly large fraction of APC (Chi square test, $p<10^{-3}$) had very long spike duration (large symbols in **Fig. 8D-F**; 10/21 APC, and 10/23 cells with very long spike duration are APC). APC with very long spike duration had strong NTA (median: 0.87, 1st-9th decile: 0.81-0.93, **Fig. 8D**) and low peak firing (median: 5 spk/s, 1st-9th decile: 2.7-11.4, **Fig. 8D**); while other APC had lower NTA (median 0.77, 1st-9th decile: 0.55-0.92, p=0.012, **Fig. 8D**) and widely distributed peak firing (median 21 spk/s, 1st-9th decile 2-56 spk/s, **Fig. 8D**).

LS cells: One fifth (20%) of cells encoded the animal's linear speed (**Fig. 8A**). LSC could fire short-duration (14/22, 64%) or long-duration (8/22, 36%) spikes (**Fig. 8F**). LS modulation amplitudes were modest (median: 0.37, 1st-9th decile: 0.24-0.59, **Fig. 8C,D**).

bioRxiv preprint doi: https://doi.org/10.1101/684464; this version posted June 27, 2019. The copyright holder for this preprint (which was not certified by peer review) is the author/funder. All rights reserved. No reuse allowed without permission.

Other responses: We also encountered a substantial (9%) fraction of EBC in the hippocampus **Fig. 8A,B**, with similar modulation amplitudes as in other areas (median: 0.63, 1st-9th decile: 0.51-0.9, **Fig. 8C**).

Theta rhythm: Theta rhythm was recorded in all animals (**Fig. 8S1**). A large fraction (53%) of all neurons was ΘP modulated, including the majority of APC (86%) and of LSC (95%) (**Fig. 8A**). Modulation amplitude was moderate (media: 0.4, 1st-9th decile: 0.2-0.71) (**Fig. 8C**).

Spiking properties: As in other regions, there was a negative correlation between mean firing rate and CV2 (**Fig. 8E**, Spearman rank correlation=-0.85, $p<10^{-10}$). Spiking duration varied widely (**Fig. 8F**): 38% of the neuronal population fired short-duration spikes (<=0.33ms trough to peak). Amongst neuron with longer-duration spikes, we observed that a large fraction (21% of the total population) fired very long-duration spikes (>0.9 ms trough to peak), and the remaining 41% fired spikes with intermediate duration. Furthermore, many neurons with >0.9ms trough to peak spike duration clustered in **Fig. 8E** (large symbols in upper left) in a group characterized by low firing rate (typically less than 4spk/s) and highly irregular (CV2>1.2).

Fimbria and fornix

We recorded neuronal responses in white matter regions located anterior and ventral to the thalamus. These regions encompass the fimbria and fornix, and convey many fibers between regions of the navigation circuit (Adelmann et al. 1996; Bubb et al. 2017). Accordingly, we found that neurons recorded in these regions encode a variety of navigation variables (**Fig. 8S2**, **Fig. 8S3**).

Preferred phase of ΘP-modulated cells

We found that the preferred phase of ΘP-modulated cells were consistent across areas, with preferred firing occurring preferentially in the descending phase (i.e. between 180° and 270°, **Fig. 8S4**).

Classification of APC: comparison with other techniques

We also compared the LN model to previous techniques (Skaggs 1993; Rubin et al. 2014) that compute the spatial information (SI) or AP tuning curve and use a shuffling test to evaluate statistical significance (**Fig. 8S5**). Again we found that the LN model is less sensitive than the shuffling test (**Fig. 8S5B**). Furthermore, we found that HD tuning could easily be misinterpreted as AP tuning, as pointed out by (Peyrache et al. 2017) (**Fig. 8S5C**, left), an issue that could also affect EBC (**Fig. 8S5C**, right). Because of this, 17 to 24% of the cell populations in ATN, RSC and cingulum were incorrectly classified as APC by a conventional shuffling test. Thus, a traditional measure of spatial information combined with a shuffling test may be enough to identify APC reliably in the hippocampus, where EBC and HDC are scarce (**Fig. 8S5K**). In contrast, testing for AP responses in regions that host other cell types, such as the ATN, RSC, cingulum and parahippocampal regions requires classification methods that can control for responses to other variables, such as the LN model or techniques used in earlier studies (Muller et al. 1994; Cacucci et al. 2004 ; Rubin et al. 2014; Peyrache et al. 2017).

bioRxiv preprint doi: https://doi.org/10.1101/684464; this version posted June 27, 2019. The copyright holder for this preprint (which was not certified by peer review) is the author/funder. All rights reserved. No reuse allowed without permission.

Discussion

We used a recently developed LN model (Hardcastle and al. 2017) to analyze how neuronal activity in multiple areas of the brain's navigation network encode combination of navigation variables. As expected, the LN model identified prominent and well-known characteristics of these areas, such as the prevalence of HDC in ATN and in the postsubiculum, or place cells in the hippocampus, but it went further and revealed several novel features. We found that egocentric information is represented not only in RSC but also in ATN and in the hippocampal regions. Furthermore, we found that about 12% of ATN neurons encode the animal's allocentric position, a finding that we confirmed by re-analyzing previously published data (Peyrache et al. 2015). We recorded spiking activity from the cingulum fiber bundle and found that most units resemble ATN or RSC neurons, suggesting that spatial information encoded in these regions travels along the cingulum.

Anterior thalamic nuclei: Our recordings in the ATN consisted predominantly of antero-dorsal nuclei neurons. The presence of a large population of HDC in the ATN of rats (Taube et al. 1995; Blair and Sharp 1996; Zugaro et al. 2001; Peyrache et al. 2015,2017; Page et al. 2017) and mice (Yoder and Taube 2009) is well documented.

More surprising was the finding of a substantial population of APC, i.e. cells tuned to the animal's allocentric position, in 3 of our animals (**Fig. 6S1**) as well as in 2 animals in a previously published dataset (Peyrache et al. 2015; **Fig. 6S4**), some of which exhibited very sharp tuning (**Fig. 6S2**). Importantly, the spike waveform of most APC exhibited long trough to peak duration (>0.33 ms; **Fig. 6F** and **Fig. 6S3F**, green), indicating that they were not likely fibers traversing the ATN. It also rules out the possibility that these cells may have been recorded in the fimbria, just dorsal to the thalamus, and erroneously classified as ATN cells. Indeed, although the fimbria contains 12% of APC (**Fig. 8S2A**), these cells typically exhibit short trough to peak duration (**Fig. 8S2F**). It also likely rules out the possibility that these cells were recorded in the stria medullaris. Yet, we can't resolve with complete certainty the location of these neurons. The dataset of Peyrache et al. (2015) indicates that these neurons may overlap the population of HDC in the antero-dorsal nuclei, but be more numerous lateral to the antero-dorsal nuclei, i.e. in the antero-ventral or latero-dorsal nuclei (**Fig. 6S4**). Thus, more detailed studies would be required to assess the spatial distribution of APC in the anterior thalamus.

Theta rhythm is a fundamental property of the navigation circuit, and it thought to mediate memory and planning in the hippocampus (Buzsáki and Moser 2013) and in general inter-regions communication (Maris et al. 2016). Previous studies (Tsanov 2010,2011) have shown that a portion of HDC in the antero-ventral nuclei of rats respond in phase with the theta-band LFP. Here we extended these results to the ATN. We found that a clear theta-band LFP was present in all animals (**Fig. 6S1E**, peak in the 5-12Hz frequency range), and that over half of HDC and most APC and EBC fired in phase with the theta rhythm.

Retrosplenial cortex and Egocentric boundary cells: We found that about half of RSC neurons encode the egocentric position of the arena's boundary. The existence of egocentric boundary cells (EBC) was proposed by Derdikman (2009), and EBC were recently identified in the entorhinal cortex (Wang et al. 2018) and RSC (Carstensen et al. 2018; Hinman et al. 2019). Several studies have described HDC in the

bioRxiv preprint doi: https://doi.org/10.1101/684464; this version posted June 27, 2019. The copyright holder for this preprint (which was not certified by peer review) is the author/funder. All rights reserved. No reuse allowed without permission.

RSC (Chen et al. 1994a,b; Cho et al. 2001; Jacob et al. 2017; Lozano et al. 2017). Here we found that, although 28% of RSC cells were tuned to HD, the majority of these were in fact EBC with weaker but significant responses to HD, such that only 4% of RSC cells were classified as HDC. Over half of EBC in the RSC were significantly tuned to HD, which suggests that the RSC may be involved in combing multiple reference frames (see Clark et al. 2018). Note that the population responses appear similar in the granular (animal AA2; **Fig. 7S1**) and dysgranular (other animals; **Fig. 7S1**) cortices.

Cingulum fiber bundle: The cingulum connects several areas of the navigation system (Domesick 1970; van Groen and Vyss 1990,1995, Bubb et al. 2017, 2018). It conveys anterior thalamic projections to the RSC and parahippocampal regions and RSC projections to the cingulate cortex and parahippocampal regions. The cingulum also carries projections from the subiculum to the RSC and parahippocampal regions, however it is unlikely that these fibers were recorded since most of our cingulum recordings were performed at the level of the anterior part of the RSC, i.e. ~0.2mm posterior to Bregma. Lesion studies have confirmed that the cingulum is involved in using allocentric cues for spatial navigation (see Bubb et al. 2018 for review), suggesting that it conveys spatial information.

The present recordings from the cingulum identified large fractions of HDC and EBC that are strikingly similar to their ATN and RSC counterparts. In particular, many HDC in the cingulum exhibited the high firing rate and NTA (**Fig. 7S4D**) that are typical of ATN HDC (**Fig. 6D**) and would scantly be distinguishable from ATN units when examined online. Likewise, EBC recorded in the cingulum were similar to those encountered in RSC (**Fig. 7D**, **Fig. 7S4D**), but as expected exhibited shorter waveforms (Robbins, 2013). We found only weak theta-band LFP in the cingulum, and few cells fired in phase with it. In contrast, half of the cells in the ATN, which projects though the cingulum, are theta-modulated. It is possible that LFP recorded in the cingulum may have diffused from nearby structures, e.g. the lateral septum or the hippocampus, and be at least partially incoherent with LFP in the ATN. In this case, spikes originating from the ATN and recorded in the cingulum would be phase-locked with LFP in the ATN, but not with LFP measured in the cingulum. Alternatively, it is possible that only ATN units that do not modulate with theta-band LFP project in the cingulum. Although many HDC recorded in the cingulum resemble ATN HDC, it should be noted that other anterior thalamic nuclei, some of which contain HDC (i.e. the antero-ventral; Tsanov 2010,2011; and antero-medial; Mizumori and Williams 1993), also project through the cingulum and that these projections may have been recorded in this study.

Hippocampus: As expected, we found a population of APC in the hippocampus that matched the typical profile of hippocampal place cells in rats (O'Keefe 1971, 1796) and mice (Muzzio, 2009; Jeantet, 2012; Kinsky, 2018), i.e. high spatial selectivity, low average firing, and long spiking duration (**Fig. 8D-F**). We also recorded a population of cells that were tuned to linear speed. In agreement with a recent study (Góis and Tort 2018), these cells often exhibited fast spiking and short spike durations.

Fimbria and fornix: We recorded neural activity in the white matter regions located anterior and ventral to the hippocampus (**Fig. 8S3**). These regions contain a variety of fiber tracks, including projections from the septal nuclei and entorhinal cortex as well as commissural projections (Adelmann et al. 1996; Bubb et al. 2017). We found that the fimbria contains a variety of spatially modulated cells.

bioRxiv preprint doi: https://doi.org/10.1101/684464; this version posted June 27, 2019. The copyright holder for this preprint (which was not certified by peer review) is the author/funder. All rights reserved. No reuse allowed without permission.

In particular, 16% of recorded cells were HDC (**Fig. 8S2A**) with large firing rate and NTA (**Fig. 8S2D**) and resembled ATN HDC, although that ATN is not known to project through the fimbria. In many animals (e.g. H71M, I29M, VR8, **Fig. 8S3**), these HDC were recorded directly above the thalamus. This reveals a challenging methodological point for neuronal recording targeting, for instance, the antero-dorsal thalamic nuclei, since it shows that lowering electrodes until characteristic HDC are observed is not sufficient to reach these nuclei consistently, and emphasizes the importance of histological confirmation of recording locations. We considered the eventuality that those HDC recorded directly above the thalamus may in fact be ATN cells whose location would have been misidentified. However, we rejected this possibility on the basis that HDC were observed consistently in animals where recording locations were placed well above the thalamus (e.g. H63M, H74M, I12M; **Fig. 8S3**).

The fimbria also contained a large population (12%) of APC (**Fig. 8S2A**). These firing properties of these cells (**Fig. 8S2A**) were clearly distinct from those of typical hippocampal place cells (**Fig 8A**). Because of the multiplicity of fiber tracks surrounding the hippocampus, it is difficult to formulate hypotheses regarding the nature of fimbria and fornix cells based on extracellular recording alone. Yet, our observations provide guidance for future studies, for instance by pointing out the possibility of mistaking the fimbria for the ATN based on the presence of HDC.

Tetrode recordings in the white matter: Although tetrodes are rarely used to target fibers, previous studies (Robbins et al. 2013) have shown that they can be used to record axonal spikes. We found that spiking could readily (and, in fact, remarkably easily) be recorded in the cingulum, and we also recorded consistently in the fimbria. Although fiber tracks traveling in the fimbria are difficult to identify, the cingulum is anatomically well delimited, and our study demonstrates that systematic investigations of information transmitted along this bundle is feasible.

Conclusion

The LN model (Harcastle et al. 2018) offers a more robust way to investigate neurons responses recorded in areas of the brain's navigation system by allowing to test for multiple variables at once while proving remarkably immune to pitfalls such as overfitting. Our study provides a new picture of the information encoded by ATN and RSC cells as well as their output bundle, while re-visiting the responses in the anterior hippocampus and the neighboring white matter areas, and may serve as a guide for future investigations in these areas.

bioRxiv preprint doi: https://doi.org/10.1101/684464; this version posted June 27, 2019. The copyright holder for this preprint (which was not certified by peer review) is the author/funder. All rights reserved. No reuse allowed without permission.

Methods

Animals

A total of 22 male adult mice (20 C57BL/6; 1 nNOS-ChR2 BAC C57BL/6 transgenic mouse: VR8), 3-6 months old, were used in this study. We implanted a head-restraining bar and a microdrive/tetrode assembly under general anesthesia (Isoflurane) and stereotaxic guidance. Animals were single-housed on a reversed [12/12] light/dark cycle. Experimental procedures were conducted in accordance with US National Institutes of Health guidelines and approved by the Animal Studies and Use Committee at Baylor College of Medicine (protocol n°AN-5995).

Neuronal recordings

Neurons were recorded using 6 (animals AA1/AA2/AA18/AA20), 5 (animal VR8) or 4 (all other animals) tetrode bundles constructed with platinium-iridium wires (17 micrometers diameter, polyimide-insulated, California Fine Wire Co, USA) and platinum-plated plated for a target impedance of 200kΩ using a Nano-Z (Neuralynx, Inc) electrode plater. Tetrodes were cemented to a guide tube (26-gauge stainless steel) and connected to a linear EIB (Neuralynx EIB/36/PTB). The tetrode and guide tube were attached to the shuttle of a screw microdrive (Axona Ltd, St Albans, UK) allowing a travel length of ~5mm into the brain.

Tetrodes were positioned under stereotaxic guidance. We targeted the ATN by implanting 0.2mm posterior and 0.7mm lateral relative to Bregma, and placing the tetrodes at an initial depth of 1.8mm relative to the surface of the cortex. The cingulum was targeted by implanting at the same coordinates but at an initial depth of 1.2mm (except for one animal, AA0, where the cingulum was reached 2mm posterior to Bregma). The anterior hippocampus and was targeted by implanting 0.6mm posterior and 0.7mm lateral relative to Bregma. Recordings in the fimbria were obtained along the track of electrodes targeting the hippocampus, ATN or cingulum. The RSC was targeted by implanting 2mm posterior and 0.07mm (AA2/AA18), 0.5mm (AA20) or 0.7mm (AA1) lateral relative to Bregma and placing the electrodes at the surface of the cortex.

At the end of the study, the animals underwent transcardial perfusion with 4% paraformaldehyde (PFA). The brains were postfixed in 4% PFA and then transferred to 30% sucrose overnight. Brain sections (40µm) were stained (Nissl or neutral red staining), and examined using bright-field microscopy to localize tetrode tracks.

Recording procedure

We recorded neural activity while animals explored a circular arena (50cm diameter, 30cm height). Recordings were performed in 8-minutes sessions. The walls of the arena where white, with a black cue card covering an angle of 45°. Illumination was provided by a LED strip lining the top of the white section of the arena's inner wall. The tetrodes were connected to a tethered head stage that included two LEDs (1 red and one infra-red, 4 cm apart) for optical tracking (Cineplex, Plexon Inc.). Broadband neuronal data were acquired at 22 kHz using a MAP system (Plexon Inc.) and stored for offline analysis. Spike sorting was performed manually based on trough and peak spike amplitude and principal component analysis, using a custom Matlab script. Data was stored on a custom database programmed using Datajoint (Yatsenko et al. 2015).

Data analysis

bioRxiv preprint doi: https://doi.org/10.1101/684464; this version posted June 27, 2019. The copyright holder for this preprint (which was not certified by peer review) is the author/funder. All rights reserved. No reuse allowed without permission.

We used optical head tracking data to compute the following variables, which were divided into bins to fit the LN model: (1) Allocentric position of the head (AP) in 2D, which ranged from -25 to 25cm in each dimension, and was binned using a 12x12 grid. Note that AP is always included in a 25cm radius circle, since the arena was circular, and therefore the corners of the 12x12 were never covered. However, the LN model is designed in such a way that adding 'empty bins' won't affect its results. (2) Egocentric position of the arena boundary (EB) was encoded in 2D, as described in **Fig. 5S1**. Similar to AP, EB ranged from -25 to 25cm, is always included in a 25cm radius circle, and was binned using a grid defined in **Fig. 5S1**. (3) Head direction (HD), which ranged from -180 to 180°. A HD of 0° corresponds to the direction of the center of the black cue card. HD was divided in 18 bins. (4) Linear speed (LS) which ranged from 0 to 30cm/s and was divided in 18 bins. (5) Angular speed (AS) which ranged from -150 to 150°/s and was divided in 18 bins. (6) Phase of the theta-band LFP (ΘP) was computed by applying a Hilbert transform to band-pass filtered (5-12Hz) LFP signals, as in Hardcastle et al. 2017. ΘP ranged from 0 to 360° and was divided in 18 bins.

Additional variables were tested but were excluded from the analysis after we determined that they didn't contribute meaningfully to neuronal responses. We tested: (1) the egocentric direction of the center of the cue card; (2) the point of the arena's boundary that the head faced, i.e. we computed the intersection of the head's forward axis and of the arena boundary and divided the arena boundary in bins, and (3) the frequency and (4) the magnitude of the LFP.

To ensure that results were robust, we excluded all recordings where AP covered less than 2/3 of the bins included in the 25cm radius circle. We verified that this criterion was sufficient to ensure that all other variables were well sampled. Two animals (H62M, H65M) were excluded from the analysis because no session passed this criterion.

LN model fitting

Model fitting was performed by using the Matlab code provided by the authors of (Hardcastle et al. 2017). We optimized the code to allow fitting a large number of models (up to 9 in preliminary testing). We programmed it to fit only the models that were necessary for the forward search procedure. If n variables are tested, this procedure will test, in a worst case, n 1st order models, n-1 2nd order models, n-2 3rd order models, and so on until 1 n^{th} order model; and the procedure will generally terminate earlier. Therefore, fitting only these models instead of all possible models reduces the complexity from 2^n-1 in all cases to n.(n+1)/2 in the worst case.

The LN model scores each model based on a log-likelihood measure. When a cell was recorded during multiple sessions, the models were fitted to each session separately, and the resulting log-likelihood averages across sessions.

Note that, when a model fits continuous firing rates as the LN model does (as opposed to firing rate averaged across several trials), its coefficient of correlation will be heavily affected by the neuron's firing variability, especially in the case of sparsely firing neurons such as hippocampal place cells. Since the LN's model statistical analyses are based on log-likelihood, and comparing coefficients of correlation across cell types and areas would easily be misleading, we opted not to report coefficients of correlation.

Shuffling test for HD and AP tuning

We also quantified HD tuning by computing the mean vector length |R| of the experimental HD tuning curve. HD tuning curves were computed as an histogram FR(HD) with a bin width of 20° and smoothed

bioRxiv preprint doi: https://doi.org/10.1101/684464; this version posted June 27, 2019. The copyright holder for this preprint (which was not certified by peer review) is the author/funder. All rights reserved. No reuse allowed without permission.

using a Gaussian kernel (standard deviation 15°). $|R|$ was computed as $|R| = R = c.\Sigma FR(HD)*\exp(-i*HD)/\Sigma FR(HD)$ with $c = 3.6*\pi/180/2/\sin(1.8)$ (Zar, 1998).

We quantified AP tuning of the experimental AP tuning curve by computing the spatial information SI. We divided the area in pixels (2.5cm width, Bjerknes et al. 2018) as computed $SI = \Sigma p_i.FR_i/FR_{avg}.\log_2(FR_i/FR_{avg})$, where FR_i is the firing rate in the ith pixel, FR_{avg} the average firing rate, and p_i the probability of being in the ith pixel.

We implemented a shuffling test to assess the significance of $|R|$ and SI. For each cell, we generated 1000 samples by shifting the spikes train by a random value of at least ±10s and we recomputed $|R|$ and SI. The un-shuffled values of $|R|$ and SI were considered significant if the exceeded 99% of the shuffled values.

Additional data from Peyrache et al. 2015, 2017

In order to supplement our recordings in the ATN, we analyzed published recordings (Peyrache et al. 2015, 2017) performed in the ATN of 6 mice (named AP12, AP17, AP20, AP24, AP25, AP28, AP32 here, corresponding to Mouse12, Mouse17, etc in the original dataset), as well as in the post-subiculum of 3 mice (AP24, AP25, AP28) while animals walked freely in a rectangular arena (53x46 cm). We included a total of 39 sessions where animals covered the arena uniformly. We selected the shanks in which most neurons were recorded, which likely correspond to the antero-dorsal nuclei and their immediate vicinity, for population analysis (see **Fig. 6S3**, **Fig. 6S4**).

bioRxiv preprint doi: https://doi.org/10.1101/684464; this version posted June 27, 2019. The copyright holder for this preprint (which was not certified by peer review) is the author/funder. All rights reserved. No reuse allowed without permission.

References

1. Adelmann, G., Deller, T., & Frotscher, M. (1996). Organization of identified fiber tracts in the rat fimbria-fornix: an anterograde tracing and electron microscopic study. Anatomy and embryology, 193(5), 481-493.
2. Barry, J. M. (2015). Axonal activity in vivo: technical considerations and implications for the exploration of neural circuits in freely moving animals. *Frontiers in neuroscience*, *9*, 153.
3. Bjerknes, T. L., Dagslott, N. C., Moser, E. I., & Moser, M. B. (2018). Path integration in place cells of developing rats. *Proceedings of the National Academy of Sciences*, 201719054.
4. Blair, H. T., & Sharp, P. E. (1996). Visual and vestibular influences on head-direction cells in the anterior thalamus of the rat. Behavioral neuroscience, 110(4), 643.
5. Bubb, E. J., Metzler-Baddeley, C., & Aggleton, J. P. (2018). The cingulum bundle: Anatomy, function, and dysfunction. *Neuroscience & Biobehavioral Reviews*.
6. Bubb, E. J., Kinnavane, L., & Aggleton, J. P. (2017). Hippocampal–diencephalic–cingulate networks for memory and emotion: An anatomical guide. *Brain and neuroscience advances*, *1*, 2398212817723443.
7. Buzsáki, G., & Moser, E. I. (2013). Memory, navigation and theta rhythm in the hippocampal-entorhinal system. Nature neuroscience, 16(2), 130.
8. Cacucci, F., Lever, C., Wills, T. J., Burgess, N., & O'Keefe, J. (2004). Theta-modulated place-by-direction cells in the hippocampal formation in the rat. *Journal of Neuroscience*, *24*(38), 8265-8277.
9. Carstensen, L. C., Alexander, A. S., Hinman, J. R., & Hasselmo, M. E. (2018) Spatial correlates of the retrosplenial cortex during free exploration. Program No. 508.18. 2018 Neuroscience Meeting Planner. San Diego, CA: Society for Neuroscience, 2018. Online.
10. Clark, B. J., Simmons, C. M., Berkowitz, L. E., & Wilber, A. A. (2018). The retrosplenial-parietal network and reference frame coordination for spatial navigation. *Behavioral neuroscience*, *132*(5), 416.
11. Chen, L. L., Lin, L. H., Green, E. J., Barnes, C. A., & McNaughton, B. L. (1994a). Head-direction cells in the rat posterior cortex. Experimental Brain Research, 101(1), 8-23.
12. Chen, L. L., Lin, L. H., Barnes, C. A., & McNaughton, B. L. (1994b). Head-direction cells in the rat posterior cortex. II. Contributions of visual and ideothetic information to the directional firing. Experimental brain research, 101(1), 24-34.
13. Cho, J., & Sharp, P. E. (2001). Head direction, place, and movement correlates for cells in the rat retrosplenial cortex. Behavioral neuroscience, 115(1), 3.
14. Derdikman, D. (2009). Are the boundary-related cells in the subiculum boundary-vector cells?. *Journal of Neuroscience*, *29*(43), 13429-13431.
15. Finkelstein, A., Derdikman, D., Rubin, A., Foerster, J. N., Las, L., & Ulanovsky, N. (2015). Three-dimensional head-direction coding in the bat brain. *Nature*, *517*(7533), 159.
16. Góis, Z. H. T., & Tort, A. B. (2018). Characterizing Speed Cells in the Rat Hippocampus. *Cell reports*, *25*(7), 1872-1884.

bioRxiv preprint doi: https://doi.org/10.1101/684464; this version posted June 27, 2019. The copyright holder for this preprint (which was not certified by peer review) is the author/funder. All rights reserved. No reuse allowed without permission.

17. Hardcastle, K., Maheswaranathan, N., Ganguli, S., & Giocomo, L. M. (2017). A multiplexed, heterogeneous, and adaptive code for navigation in medial entorhinal cortex. *Neuron*, *94*(2), 375-387.

18. Hinman, J. R., Chapman, G. W., & Hasselmo, M. E. (2019) Neuronal representation of environmental boundaries in egocentric coordinates. *Nature Communications, 10.*

19. Jacob, P. Y., Casali, G., Spieser, L., Page, H., Overington, D., & Jeffery, K. (2017). An independent, landmark-dominated head-direction signal in dysgranular retrosplenial cortex. *Nature neuroscience*, *20*(2), 173.

20. Jeantet, Y., & Cho, Y. H. (2012). Evolution of hippocampal spatial representation over time in mice. *Neurobiology of learning and memory*, *98*(4), 354-360.

21. Kinsky, N. R., Sullivan, D. W., Mau, W., Hasselmo, M. E., & Eichenbaum, H. B. (2018). Hippocampal place fields maintain a coherent and flexible map across long timescales. *Current Biology*.

22. Kornienko, O., Latuske, P., Bassler, M., Kohler, L., & Allen, K. (2018). Non-rhythmic head-direction cells in the parahippocampal region are not constrained by attractor network dynamics. *eLife*, *7*, e35949.

23. Lozano, Y. R., Page, H., Jacob, P. Y., Lomi, E., Street, J., & Jeffery, K. (2017). Retrosplenial and postsubicular head direction cells compared during visual landmark discrimination. *Brain and Neuroscience Advances*, *1*, 2398212817721859.

24. Maris, E., Fries, P., & van Ede, F. (2016). Diverse phase relations among neuronal rhythms and their potential function. *Trends in neurosciences*, *39*(2), 86-99.

25. Mizumori, S. J., & Williams, J. D. (1993). Directionally selective mnemonic properties of neurons in the lateral dorsal nucleus of the thalamus of rats. *Journal of Neuroscience*, *13*(9), 4015-4028.

26. Muller, R. U., Bostock, E., Taube, J. S., & Kubie, J. L. (1994). On the directional firing properties of hippocampal place cells. *Journal of Neuroscience*, *14*(12), 7235-7251.

27. Muzzio, I. A., Levita, L., Kulkarni, J., Monaco, J., Kentros, C., Stead, M., ... & Kandel, E. R. (2009). Attention enhances the retrieval and stability of visuospatial and olfactory representations in the dorsal hippocampus. *PLoS biology*, *7*(6), e1000140.

28. O'Keefe, J., & Dostrovsky, J. (1971). The hippocampus as a spatial map: Preliminary evidence from unit activity in the freely-moving rat. *Brain research*.

29. O'Keefe, J. (1976). Place units in the hippocampus of the freely moving rat. *Experimental neurology*, *51*(1), 78-109.

30. Page, H. J., Wilson, J. J., & Jeffery, K. J. (2017). A dual-axis rotation rule for updating the head direction cell reference frame during movement in three dimensions. *Journal of neurophysiology*, *119*(1), 192-208.

31. Peyrache, A., Lacroix, M. M., Petersen, P. C., & Buzsáki, G. (2015). Internally organized mechanisms of the head direction sense. *Nature neuroscience*, *18*(4), 569.

32. Peyrache, A., Schieferstein, N., & Buzsáki, G. (2017). Transformation of the head-direction signal into a spatial code. *Nature communications*, *8*(1), 1752.

33. Preston-Ferrer, P., Coletta, S., Frey, M., & Burgalossi, A. (2016). Anatomical organization of presubicular head-direction circuits. Elife, 5, e14592.

bioRxiv preprint doi: https://doi.org/10.1101/684464; this version posted June 27, 2019. The copyright holder for this preprint (which was not certified by peer review) is the author/funder. All rights reserved. No reuse allowed without permission.

34. Robbins, A. A., Fox, S. E., Holmes, G. L., Scott, R. C., & Barry, J. M. (2013). Short duration waveforms recorded extracellularly from freely moving rats are representative of axonal activity. *Frontiers in neural circuits*, *7*, 181.

35. Rubin, A., Yartsev, M. M., & Ulanovsky, N. (2014). Encoding of head direction by hippocampal place cells in bats. Journal of Neuroscience, 34(3), 1067-1080.

36. Skaggs, W. E., McNaughton, B. L., & Gothard, K. M. (1993). An information-theoretic approach to deciphering the hippocampal code. In *Advances in neural information processing systems* (pp. 1030-1037).

37. Simonnet, J., Nassar, M., Stella, F., Cohen, I., Mathon, B., Boccara, C. N., ... & Fricker, D. (2017). Activity dependent feedback inhibition may maintain head direction signals in mouse presubiculum. Nature communications, 8, 16032.

38. Simonnet, J., & Fricker, D. (2018). Cellular components and circuitry of the presubiculum and its functional role in the head direction system. Cell and tissue research, 373(3), 541-556.

39. Taube, J. S. (1995). Head direction cells recorded in the anterior thalamic nuclei of freely moving rats. Journal of Neuroscience, 15(1), 70-86.

40. Tukker, J. J., Tang, Q., Burgalossi, A., & Brecht, M. (2015). Head-directional tuning and theta modulation of anatomically identified neurons in the presubiculum. Journal of Neuroscience, 35(46), 15391-15395.

41. Tsanov, M., Chah, E., Wright, N., Vann, S. D., Reilly, R., Erichsen, J. T., ... & O'Mara, S. M. (2010). Oscillatory entrainment of thalamic neurons by theta rhythm in freely moving rats. *Journal of neurophysiology*, *105*(1), 4-17.

42. Tsanov, M., Chah, E., Vann, S. D., Reilly, R. B., Erichsen, J. T., Aggleton, J. P., & O'Mara, S. M. (2011). Theta-modulated head direction cells in the rat anterior thalamus. *Journal of Neuroscience*, *31*(26), 9489-9502.

43. Wang, C., Chen, X., Lee, H., Deshmukh, S. S., Yoganarasimha, D., Savelli, F., & Knierim, J. J. (2018). Egocentric coding of external items in the lateral entorhinal cortex. *Science*, *362*(6417), 945-949.

44. Yatsenko, D., Reimer, J., Ecker, A. S., Walker, E. Y., Sinz, F., Berens, P., ... & Tolias, A. S. (2015). DataJoint: managing big scientific data using MATLAB or Python. *bioRxiv*, 031658.

45. Yoder, R. M., & Taube, J. S. (2009). Head direction cell activity in mice: robust directional signal depends on intact otolith organs. *Journal of Neuroscience*, *29*(4), 1061-1076.

46. Zar, J. H. Biostatistical Analysis 4th edn (Prentice Hall, 1998), pp.592-615.

47. Zugaro, M. B., Tabuchi, E., Fouquier, C., Berthoz, A., & Wiener, S. I. (2001). Active locomotion increases peak firing rates of anterodorsal thalamic head direction cells. Journal of Neurophysiology, 86(2), 692-702.

bioRxiv preprint doi: https://doi.org/10.1101/684464; this version posted June 27, 2019. The copyright holder for this preprint (which was not certified by peer review) is the author/funder. All rights reserved. No reuse allowed without permission.

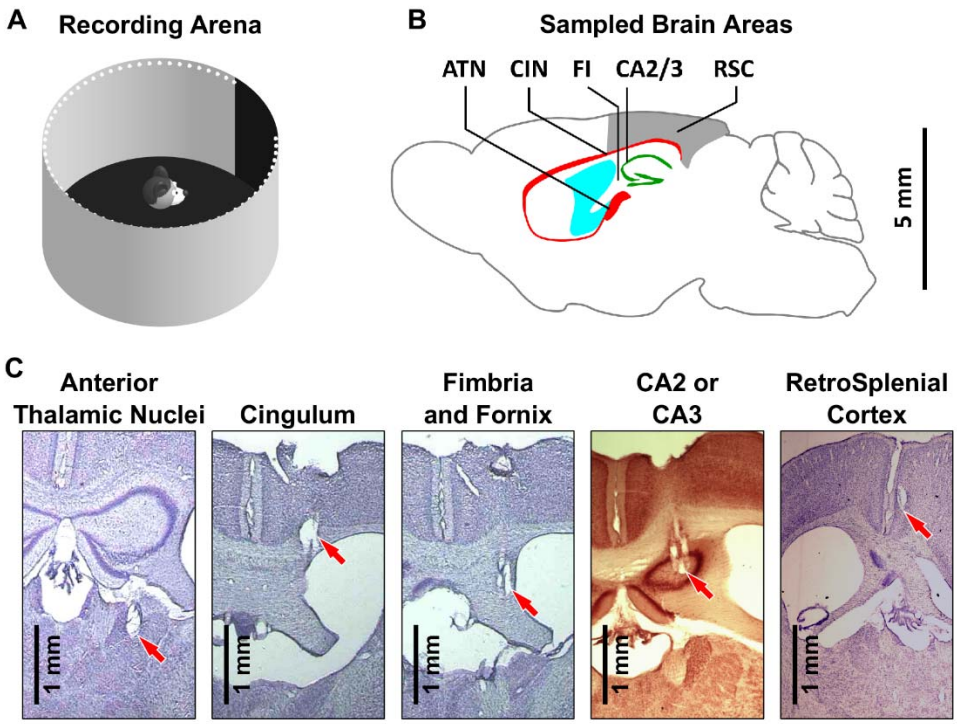

Figure 1: Overview of the experimental approach.

A: Experimental apparatus. Mice move freely in a circular arena (50 cm in diameter). A black card provides an orienting cue.

B: Sagittal section of a mouse brain at ~1 mm lateral of the midline, with all recorded regions indicated. ATN: Anterior Thalamic Nuclei. The cingulum fiber bundle (CIN) runs between the cortex and the corpus callosum. The fimbria and fornix (FI) refer here to white matter regions located around the anterior portion of the hippocampus. CA2/3: anterior portions of hippocampus. RSC: retrosplenial cortex.

C: Representative coronal sections showing tetrode track marks (red arrows) in all recorded areas (see also **Fig. 6-10S1**).

bioRxiv preprint doi: https://doi.org/10.1101/684464; this version posted June 27, 2019. The copyright holder for this preprint (which was not certified by peer review) is the author/funder. All rights reserved. No reuse allowed without permission.

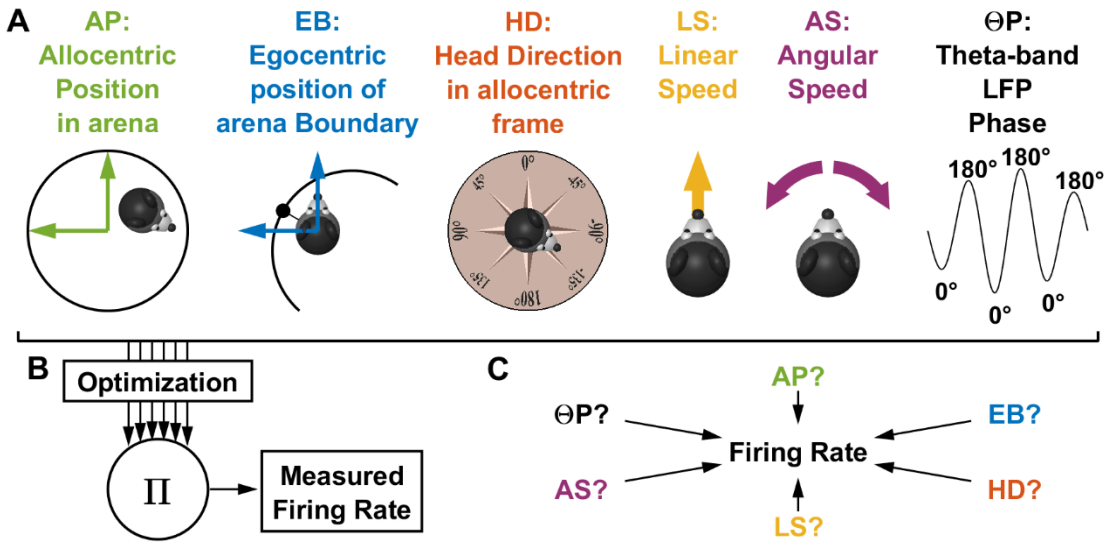

Figure 2: Overview of the LN model (Hardcastle et al. 2017).

A: Representation of the 6 variables used in the LN model. The color code is used in subsequent figures.

B: The model adjusts the tuning curve of all variables in order to fit the experimentally measured firing rate optimally, using a gradient ascent procedure, and assuming that the variables interact multiplicatively.

C: A search procedure is used to determine which variables contribute significantly to the cell's response (see Methods).

bioRxiv preprint doi: https://doi.org/10.1101/684464; this version posted June 27, 2019. The copyright holder for this preprint (which was not certified by peer review) is the author/funder. All rights reserved. No reuse allowed without permission.

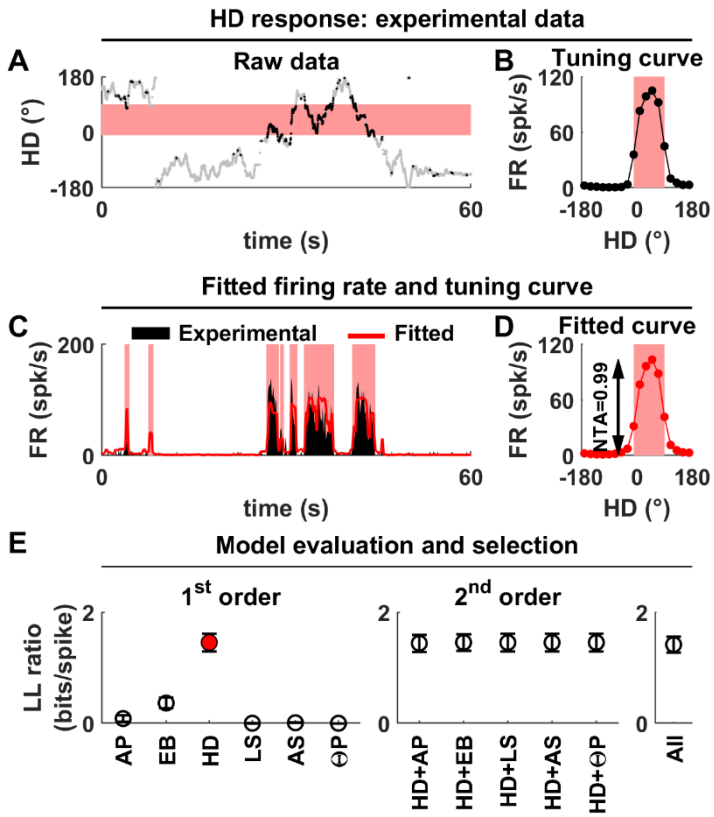

Figure 3: Example HD cell recorded in the ATN.

A: Raw data. The orientation of the animal as a function of time is shown in grey, and recorded spikes are overlaid as black dots. The cell fires preferentially when the animal's orientation is in the range of -10° to 90°, which is indicated by a pink band.

B: Traditional HD tuning curve computed by binning orientation data. The cell's preferred firing range is indicated in pink.

C: Model fit (red curve) to the cell's firing rate (black). Time periods where HD is within the preferred firing range are indicated in red. The cell fires consistently during these time periods, and this firing is accurately reproduced by the model.

D: HD tuning curve fitted by the LN model. In this simple example, the curve is identical to the experimental tuning curve in (B). Note, however, that this is not in general the case, as illustrated e.g. in Fig. 5E.

E: Illustration of the model selection procedure. Left panel: goodness of fit (LL ratio) of all 1st order models. The goodness of fit of the HD model is higher than any other model. Middle panel: goodness of fit of all 2nd order models. No model provides a significantly better fit than the HD model alone, which is therefore selected as the best model (red). Right panel: goodness of fit of the model including all variables, not significantly better than the HD model alone.

bioRxiv preprint doi: https://doi.org/10.1101/684464; this version posted June 27, 2019. The copyright holder for this preprint (which was not certified by peer review) is the author/funder. All rights reserved. No reuse allowed without permission.

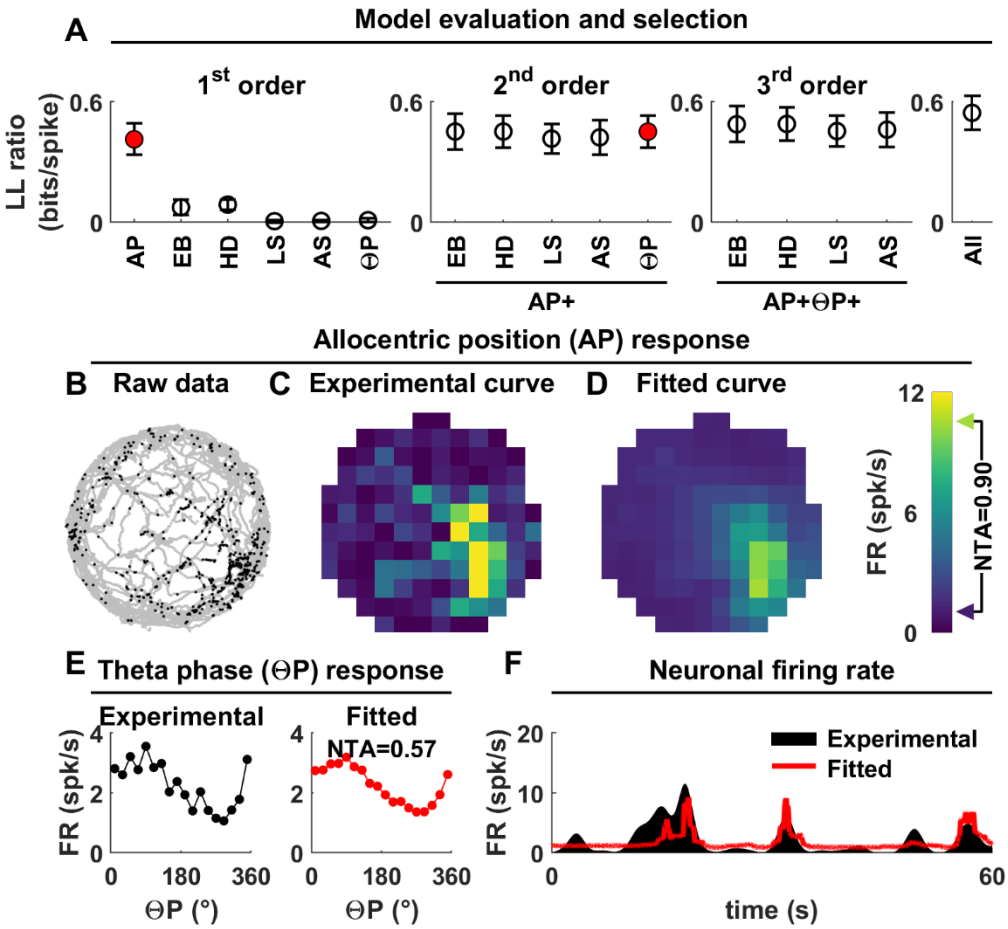

Figure 4: Example place cell recorded in the hippocampus.

A: Illustration of the model selection procedure. The LN model tested a set of 1st, 2nd and 3rd order models and selected the AP+ΘP model (red). Therefore, this cell is modulated by the animal's allocentric position (AP) and tends to fire in phase with theta-band LFP.

B: Raw data. AP recorded over time is shown in grey, and recorded spikes are overlaid as black dots.

C: Experimental AP tuning curve computed in the traditional way by binning the data and represented as a color map (the color scale is shown to the right of panel D).

D: AP tuning curve fitted by the LN model. The curve resembles the experimental curve but is smoother due to the model's smoothness constraint.

E: Experimental (left) and fitted (right) ΘP tuning. The neuron responds preferentially at a phase of ~90°, i.e. between the peak and the trough of the LFP.

F: Model fit (red curve) to a portion of the cell's firing rate (black).

bioRxiv preprint doi: https://doi.org/10.1101/684464; this version posted June 27, 2019. The copyright holder for this preprint (which was not certified by peer review) is the author/funder. All rights reserved. No reuse allowed without permission.

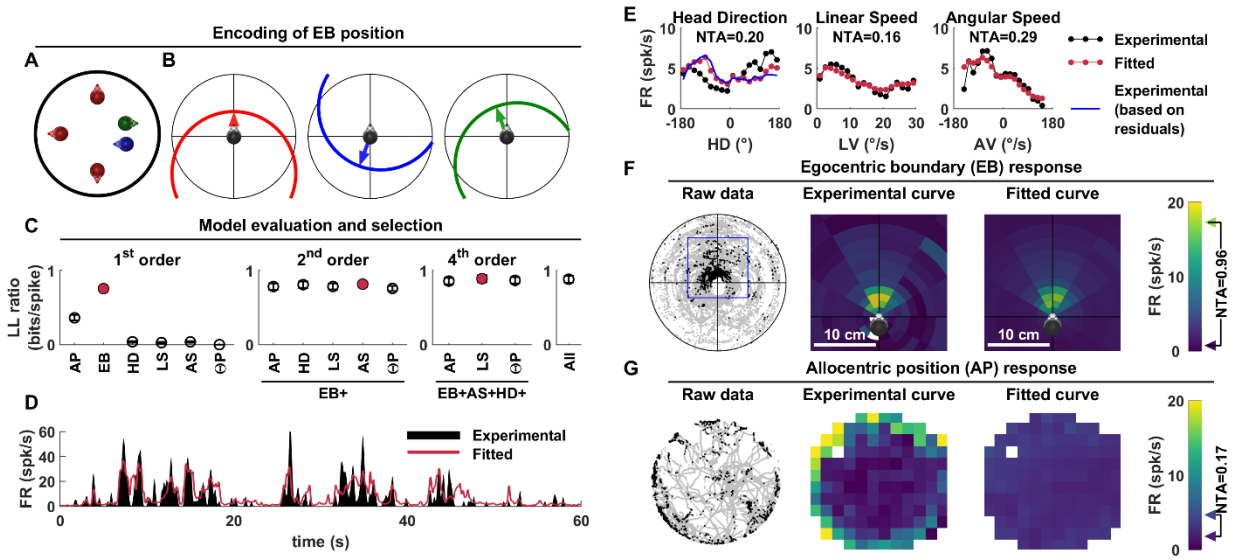

Figure 5: Example EBC recorded in RSC.

A: Encoding of the egocentric position of the arena's boundary. Five possible positions of the head within the arena are shown. The 3 heads colored in red are placed 10 cm away from the boundary and facing directly towards it. Therefore, from an egocentric perspective, their position relative to the arena are identical, although their allocentric positions are different. The green and blue colored heads are placed at a similar position, but with different orientations relative to the arena boundary.

B: Egocentric positions corresponding to the allocentric positions for the example in A. Each panel corresponds to one example head position (or multiple equivalent positions for the first panel). The arena's boundary is drawn relative to the head, and an arrow points towards its closet point. Because the arena is circular, and its radius is known, the position of the entire boundary can be known based on the position of the closest point of the boundary. Therefore, EB is represented as a 2D variable that encodes the position of the boundary closest point in egocentric coordinates (see **Fig. 5S1** for details).

C: Illustration of the model selection procedure. A set of models is tested until the 4th order model EB+HD+AV+LS is selected as best fitting.

D: Model fit (red curve) to the cell's firing rate (black). The cell tends to fire in irregular bursts, some of which are not accurately predicted by the model, although the low-frequency response is consistently captured.

E: Experimental (black) and fitted (red) HD (left), LS (middle) and AS (right) tuning curves. The experimental HD tuning curve (black) does not correspond to the fitted tuning curve (red) because the former is heavily biased by the cell's sensitivity to EB. This can be demonstrated by fitting the EB model and re-computing the experimental HD tuning curve based on the residuals of that model. The resulting curve (blue) matches the fitted tuning curve closely.

bioRxiv preprint doi: https://doi.org/10.1101/684464; this version posted June 27, 2019. The copyright holder for this preprint (which was not certified by peer review) is the author/funder. All rights reserved. No reuse allowed without permission.

F: Example cell's response to EB. Left: raw data, with EB encoded as shown in (B) and spikes overlaid as black dots (see also **Suppl. Movie 1**). Middle: experimental tuning curve. Right: fitted tuning curve.

G: Example cell's response to AP. Same legend as in Fig. 4A-C. Although the cell appears tuned to AP because it fires close to the boundarys, its response is in fact a result of its EB tuning. The fitted curve is flat, correctly reflecting the cell's absence of significant AP response.

bioRxiv preprint doi: https://doi.org/10.1101/684464; this version posted June 27, 2019. The copyright holder for this preprint (which was not certified by peer review) is the author/funder. All rights reserved. No reuse allowed without permission.

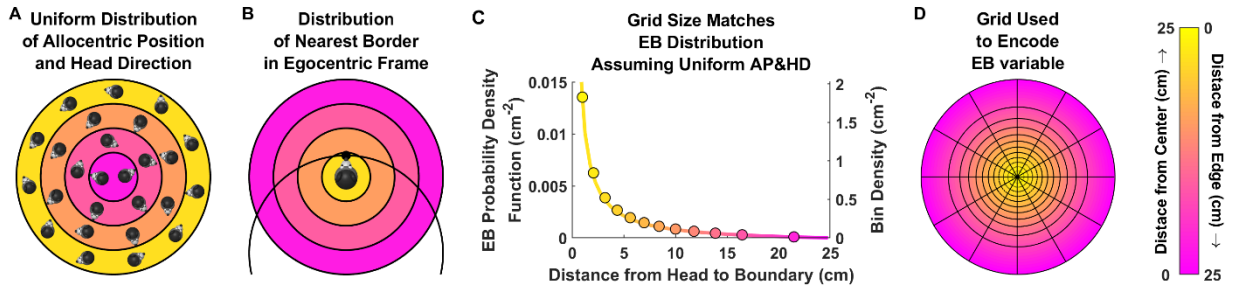

Figure 5 Supplemental 1: Encoding the EB variable.

A: Arena seen from an allocentric point of view. The arena is divided in color-coded (yellow to magenta) concentric regions. All regions have the same width; but outermost regions have a larger perimeter. Therefore, the outer regions (e.g. yellow) have a larger surface area than the innermost (e.g. magenta). If the animal explores the arena uniformly (as illustrated by the mice heads, where AP and HD are uniformly distributed), the head is more likely to be located in the yellow regions.

B: In egocentric space, the egocentric position of the nearest boundary (EB) falls inside of a circle with 25 cm radius (since the closest boundary is at most 25 cm away from the head). Points where the head is close to the boundary correspond to the (large) yellow region in A and to the (much smaller) yellow region in B. Thus, if AP is uniformly distributed in A, EB is non-uniformly distributed in B, with a higher probability of being close to the center.

C: Probability density function of EB (line), estimated by drawing a large (10^7) number of head positions where AP and HD are uniformly distributed (as in panel A; we assumed that AP can't be located closer than 0.5cm to the arena's wall to account for the animal's head size) and computing the corresponding EB. The density function is expressed in probability per cm^2, and plotted here as a function of the distance between the head and the boundary. The density is higher in proximal space (i.e. yellow region). Accordingly, we bin the egocentric space in B with a grid that has a higher density (i.e. small bins) in proximal space (dots, see panel **D**).

D: To represent EB, we created a grid that has a higher resolution in proximal space so as to match the distribution in (C). First, we computed 12 concentric zones (**Fig. 5S1D**) whose width was adjusted such that each contained $1/12^{th}$ of all samples used in C. Thus, by construction, EB is distributed uniformly across all zones. All zones were further divided into 12 angular sectors to create a grid onto which EB is uniformly distributed. The surface area of grid bins is computed and its inverse (grid density, in cm^{-2}) is shown, as a function of radius, in C. As expected, the resulting points (disks) scale with the EB density function.

bioRxiv preprint doi: https://doi.org/10.1101/684464; this version posted June 27, 2019. The copyright holder for this preprint (which was not certified by peer review) is the author/funder. All rights reserved. No reuse allowed without permission.

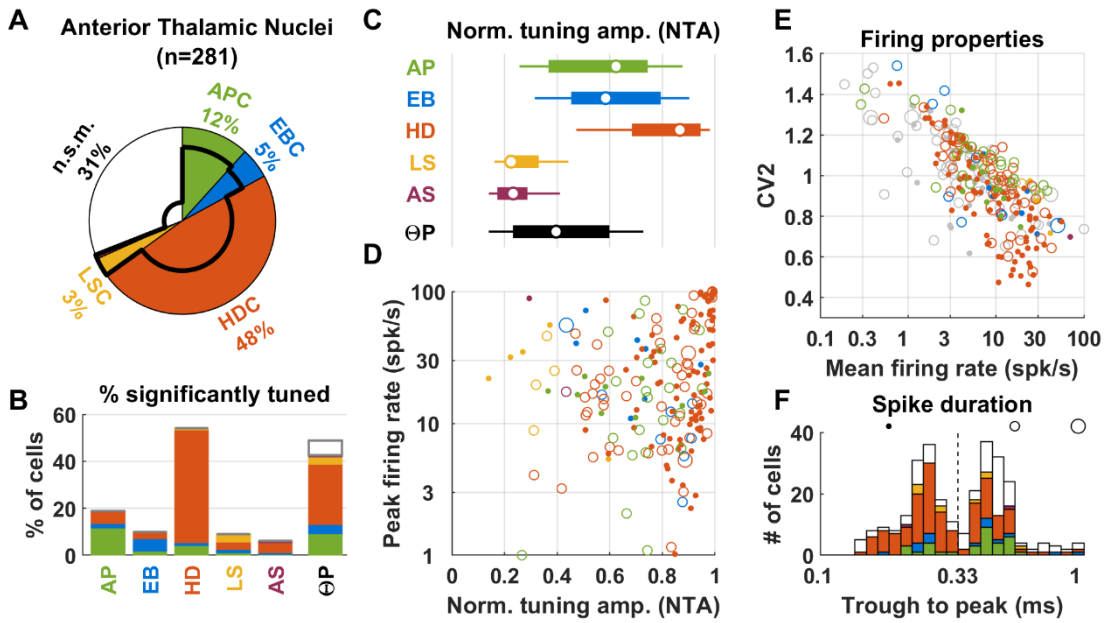

Figure 6: Population responses in the ATN. **A:** Diagram of cell classification. The proportions of APC, ABC, HDC, LSC and ASC are shown by colored sectors. Non-spatially modulated (n.s.m.) cells are represented by the white sector. In addition, the proportions of ΘP-modulated cells in each sector is represented by a black line.

B: Proportion significant tuning to all variables used. The first bar (AP) represents the percentage of cells that respond significantly to AP. However, these cells may respond more to another variable (e.g. HD) and may therefore not be classified as APC: for instance, some cells are classified as HDC and are represented by the orange portion of the bar. Subsequent bars follow the same logic. The white portion of the last bar represents the proportion of ΘP-modulated non-responsive cells.

C: Normalized response amplitude (NRA) of cells with significant modulation to AP, EB, HD, LS, AS and ΘP. Circles/bars/whiskers represent the median, upper/lower quartiles and upper/lower deciles.

D: Peak firing rate versus NRA of APC, EBC, HDC, LSC and ASC (only cells whose predominant responses is AP, EB, etc, are represented here, in contrast with panel C where all significantly tuned cells are included). Cells are color-coded based on their classification (see panels A-C for color code). The size of the symbols encodes the trough to peak spike duration (small symbols: less than 0.33ms; medium symbols: between 0.33 and 0.8ms; large symbols: more than 0.8ms).

E: Firing properties (CV2 versus mean firing rate) of ATN cells, color-coded as in panel D. Not spatially modulated cells are shown in grey.

F: Distribution of trough to peak spike duration, color-coded by cell classification. The black circle/disks illustrate the symbol size code used in panel D,E.

bioRxiv preprint doi: https://doi.org/10.1101/684464; this version posted June 27, 2019. The copyright holder for this preprint (which was not certified by peer review) is the author/funder. All rights reserved. No reuse allowed without permission.

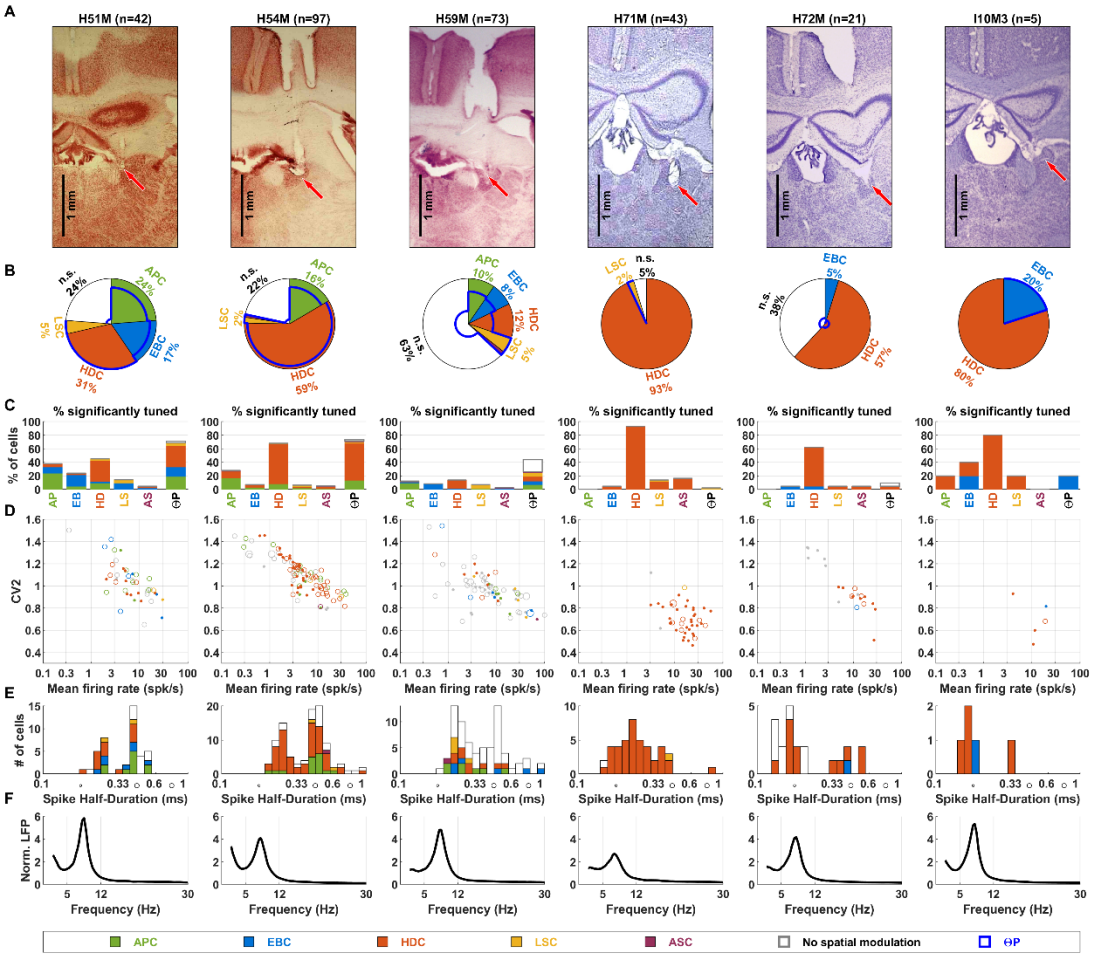

Figure 6 Supplemental 1: Recordings in the ATN of individual mice.

A: Coronal histology sections in each animal, showing the location of tetrode tracks. Tracks are predominantly located in the antero-dorsal nuclei, although they may possibly have contacted neighboring regions; e.g. antero-ventral nucleus in H71M; latero-dorsal nucleus in H72M; stria medullaris in H51M.

B: Venn diagram showing the proportions of all cell types and of ΘP-modulated cells, as in **Fig. 6A**. HDC were recorded in all animals. Clear populations (>5%) of APC and EBC were recorded in 3 and 4 animals respectively.

C: Proportion significant tuning to all variables, as in **Fig. 6B**.

D: Firing properties (CV2 versus mean firing rate) of recorded cells, as in **Fig. 6E**.

E: Distribution of trough to peak spike duration, as in **Fig. 6F**.

F: Average (over all electrodes and recording sessions) LFP power spectrum. A clear theta-band LFP, peaking between 5 and 12Hz, was observed in all animals.

bioRxiv preprint doi: https://doi.org/10.1101/684464; this version posted June 27, 2019. The copyright holder for this preprint (which was not certified by peer review) is the author/funder. All rights reserved. No reuse allowed without permission.

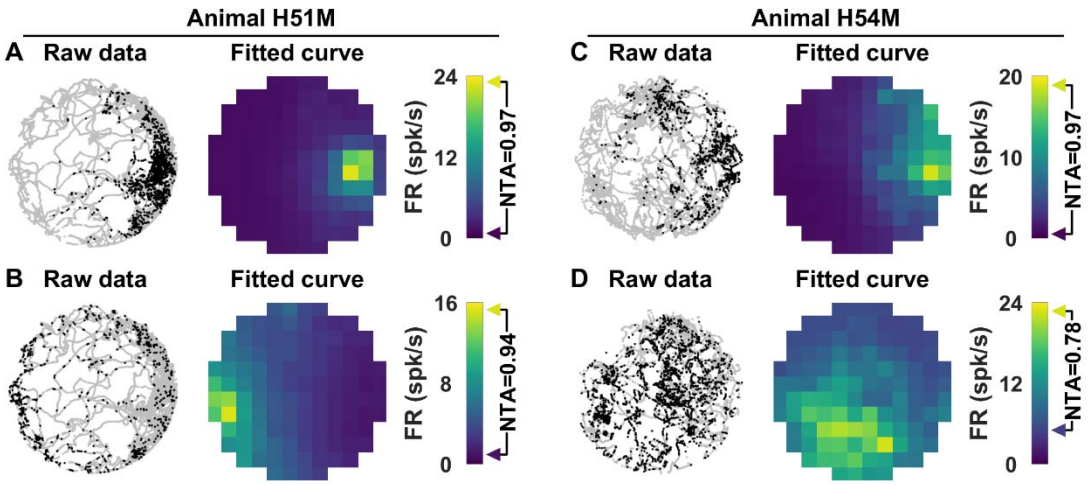

Figure 6 Supplemental 2: Example APC in the ATN. The response of 4 ATN APC are shown. Left panels: raw data, showing the recorded head position (grey) and spikes overlaid as black dots. Right panels: fitted tuning curve represented as color maps. The NTA is indicated on the color scale.

bioRxiv preprint doi: https://doi.org/10.1101/684464; this version posted June 27, 2019. The copyright holder for this preprint (which was not certified by peer review) is the author/funder. All rights reserved. No reuse allowed without permission.

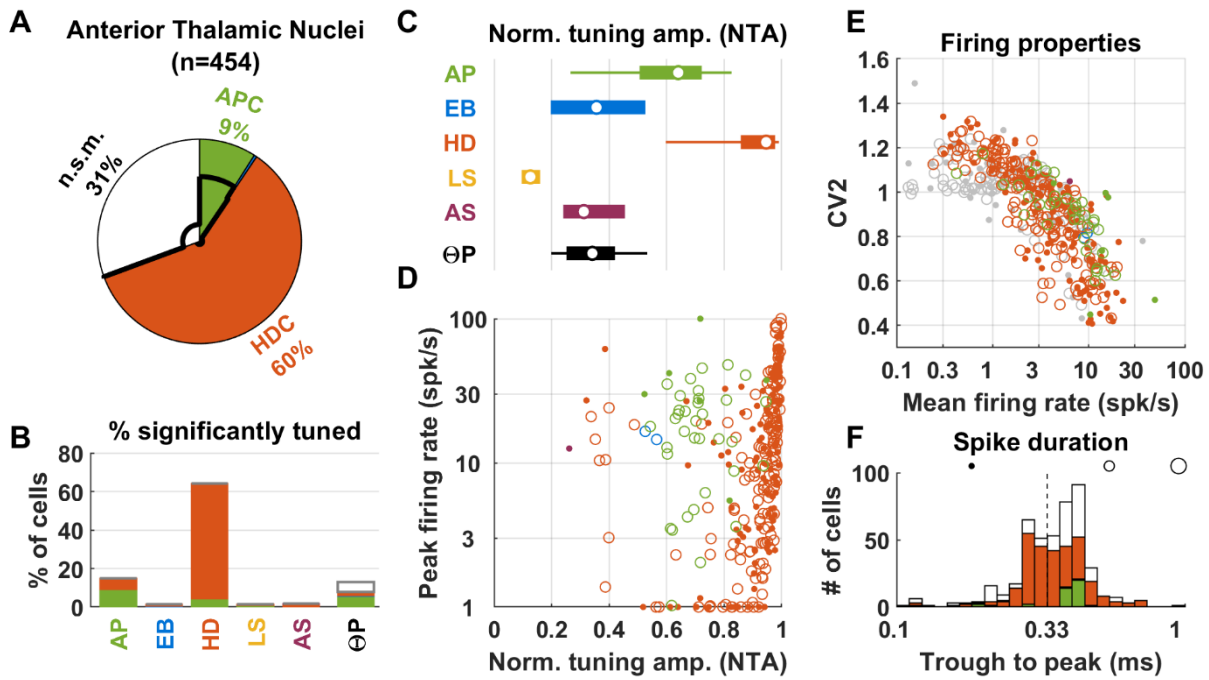

Figure 6 Supplemental 3: Population responses in the ATN from previously published data (Peyrache et al. 2015). Same legend as in Fig. 6.

In agreement with our recordings, a large fraction (60%, panel A) of ATN cells are classified as HDC. HD responses have high NTA (panel C; median = 0.95; 1st – 9th decile: 0.6-0.99). HDC could reach high NTA and peak firing (e.g. NTA>0.9, peak firing > 30 spk/s), similar to our recordings.

We observed that HDC with very low peak firing (e.g. <3 spk/s) amounted to a larger fraction of the population than in our recordings (23% vs. 3%; panel D), and similarly HDC with very low mean firing (e.g. <1 spk/s; panel E) were frequent in these recordings (14% vs. 0%). It is possible that the longer recording durations used in Peyrache et al. 2015 (30 min foraging, total recordings amounting to several hours) made it easier to identify clusters of spikes occurring at low frequencies.

We also observed that 9% of cells were classified as APC (panel A; see also **Fig. 6S4**). The NTA of AP responses in Peyrache et al.'s dataset (median = 0.64; 1st – 9th decile: 0.27-0.83) closely matched the value found in our study (median = 0.63; 1st – 9th decile: 0.26-0.88; Wilcoxon rank sum test: p=0.99). Likewise, the distribution of APC's peak firing rates (median = 20 spk/s; 1st – 9th decile: 3.6-41) matched our recordings (median = 17 spk/s; 1st – 9th decile: 5-54; Wilcoxon rank sum test: p=0.99).

Similar to our recordings, the distribution of spike duration was bimodal (panel F), with 39 and 61% of cells exhibiting short- and long-duration spikes, respectively. Note that the two peaks of the bimodal distribution were not as distinct (compare with **Fig. 6F**); possibly because of difference between the type of electrodes and filtering used in our study and Peyrache et al.'s recordings which may have influenced the spike's apparent duration.

bioRxiv preprint doi: https://doi.org/10.1101/684464; this version posted June 27, 2019. The copyright holder for this preprint (which was not certified by peer review) is the author/funder. All rights reserved. No reuse allowed without permission.

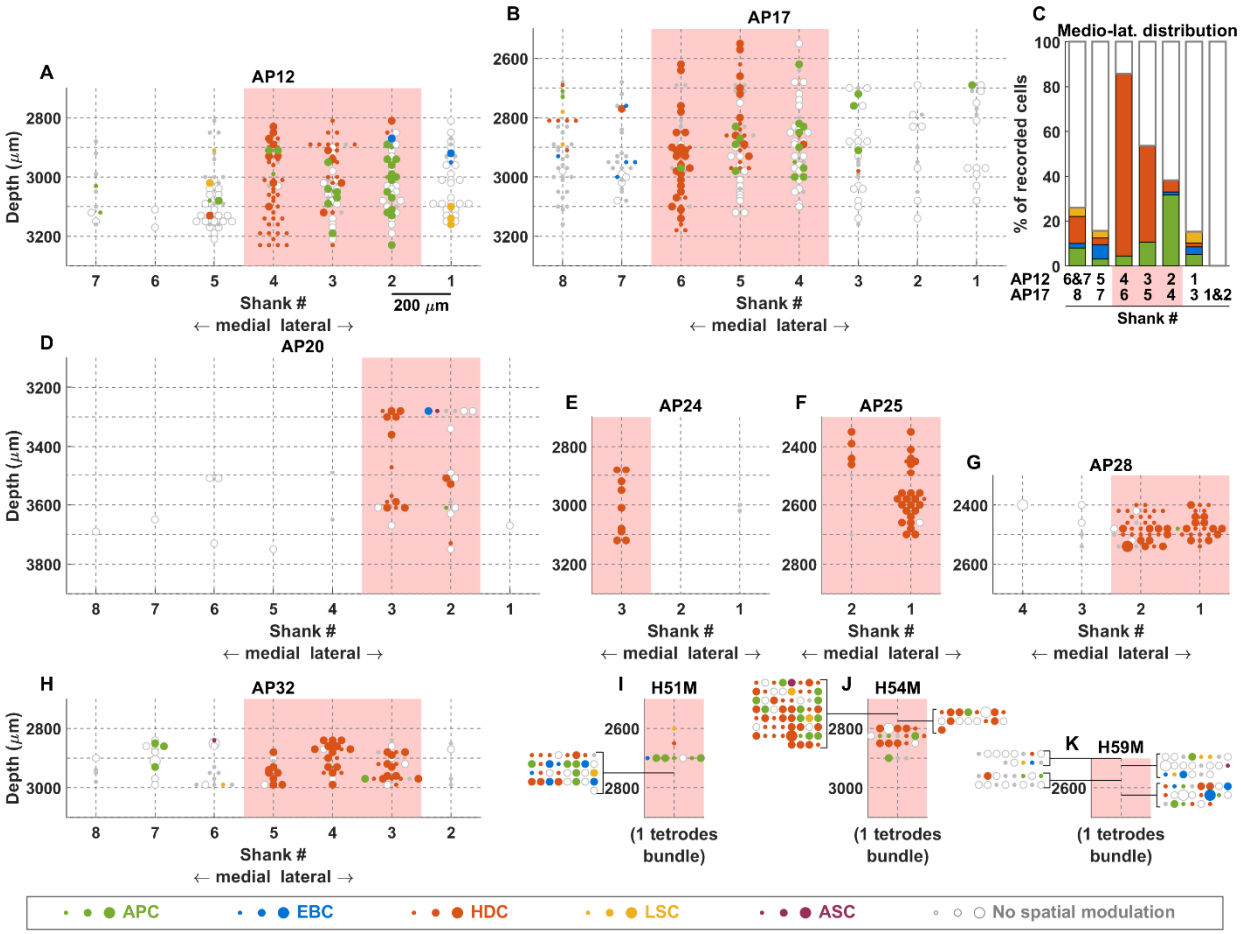

Figure 6 Supplemental 4: Spatial distribution of neuronal response types in ATN.

Neuronal responses in Peyrache et al. 2015 were recorded using multiple-shank probes (200 µm spacing between shanks) that were lowered in the brain between recording sessions, thus covering a large 2D space. In this figure, we map the neurons recorded in this study, with particular focus on the relative location of HDC and APC.

A,B: Location of neurons recorded in animals AP12 and AP17, where most APC were found. Neurons are located based on their depth relative to Bregma (ordinate axis) and shank number (shanks are distributed along the medio-lateral axis). Neurons recorded on a single shaft are staggered laterally for better visualization. The pink zone indicates the region where most responsive neurons were recorded, which likely includes the antero-dorsal nucleus and its immediate vicinity. Only neurons recorded in this region were included in the population analysis in **Fig. 6S3**. We observe that HDC (orange) tend to cluster in the medial part of this region, whereas APC (green) tend to cluster in the lateral part.

C: Percentage of cells classified in all categories as a function of medio-lateral position in animals AP12 and AP17. The shanks were shifted in each animal to align the presumed location of the antero-dorsal nuclei, indicated in pink. HDC were predominant (82% of recorded cells) in shanks #4 (AP12) and #6 (AP17) (leftmost bar), whereas APC were found more often in shanks #2 (AP12) and #4 (AP17) (32% of

bioRxiv preprint doi: https://doi.org/10.1101/684464; this version posted June 27, 2019. The copyright holder for this preprint (which was not certified by peer review) is the author/funder. All rights reserved. No reuse allowed without permission.

recorded cells). Intermediate proportions of APC (11%) and HDC (43%) were found in-between. This indicates that HDC and APC are spatially segregated in ATN, with some overlap in these populations.

D,H: Location of neurons recorded in other animals by Peyrache et al. 2015.

I,K: Location of neurons in the present study, for animals where APC were present in the ATN. Large groups of cells recorded at a single location are represented at the side of the graph for readability. Recordings in these three animals were restricted to a single medio-lateral position, since we used only one tetrode bundle and a narrow range of depths (spanning less than 200 µm in all animals). With these recordings, we observe that HDC and APC are commonly recorded at a single location. This indicates that these recordings were performed in a region where APC and HDC overlap.

bioRxiv preprint doi: https://doi.org/10.1101/684464; this version posted June 27, 2019. The copyright holder for this preprint (which was not certified by peer review) is the author/funder. All rights reserved. No reuse allowed without permission.

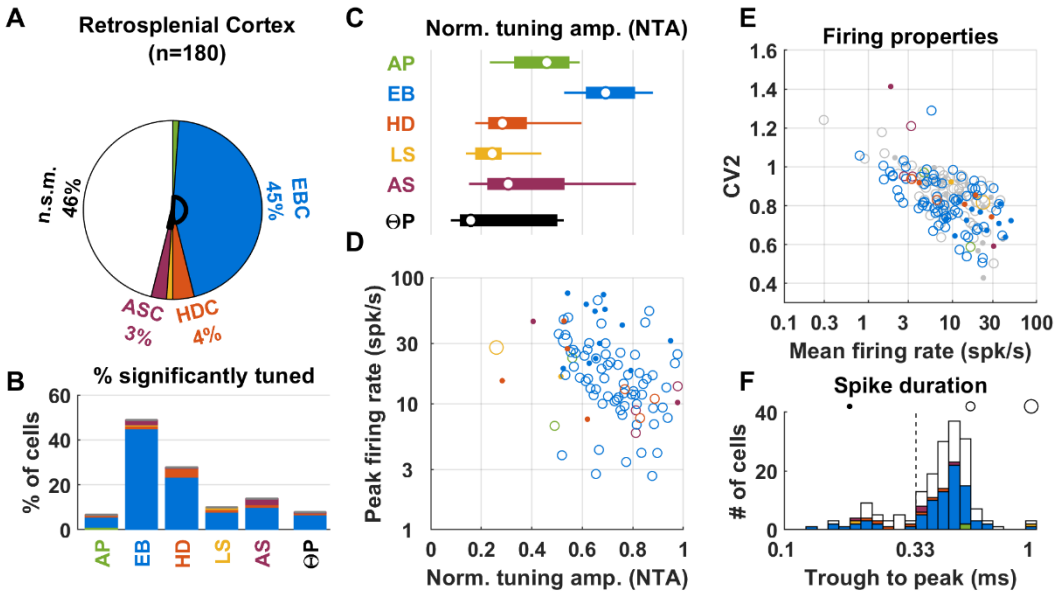

Figure 7: Population response in the RSC. Same legend as in **Fig. 6**.

bioRxiv preprint doi: https://doi.org/10.1101/684464; this version posted June 27, 2019. The copyright holder for this preprint (which was not certified by peer review) is the author/funder. All rights reserved. No reuse allowed without permission.

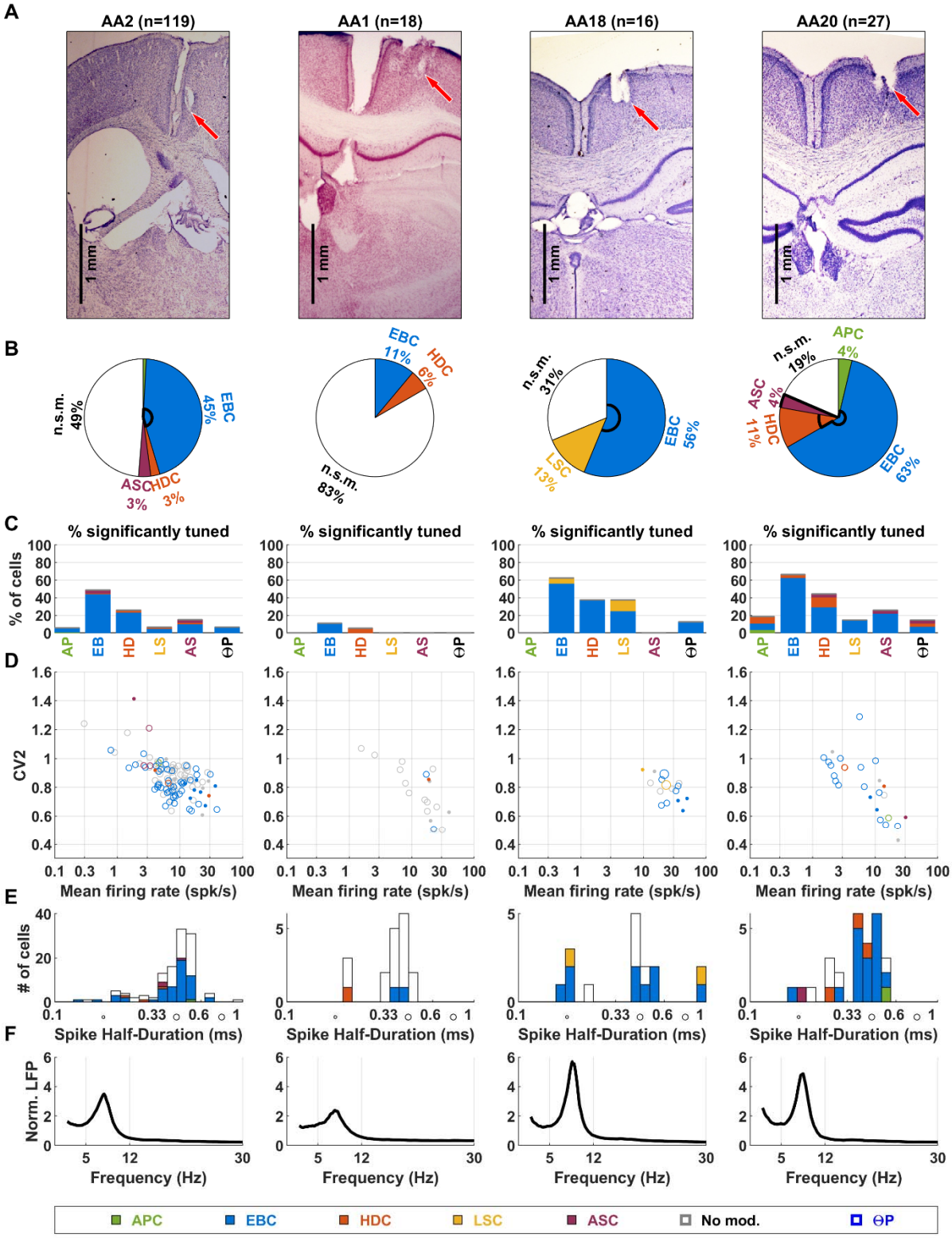

Figure 7 Supplemental 1: Recordings in the RSC of individual mice. Same legend as in **Fig. 6 Suppl. 1**. Animal AA2 was implanted in the granular cortex, and AA1, AA18 and AA20 in the dysgranular cortex.

bioRxiv preprint doi: https://doi.org/10.1101/684464; this version posted June 27, 2019. The copyright holder for this preprint (which was not certified by peer review) is the author/funder. All rights reserved. No reuse allowed without permission.

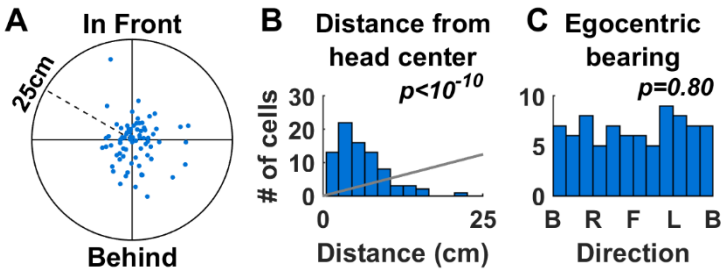

Figure 7 Supplemental 2: Spatial properties of EBC in RSC.

A: Distribution of the preferred position of EBC. The preferred position refers to the egocentric location of the nearest boundary (as in **Fig. 2, 5**) at which the cell fires most, and is plotted in polar coordinates, with the distance from the origin representing the distance from the head, and the direction representing the egocentric bearing to the nearest point (i.e. in front of the head, to the right, behind the head, or to the left).

B: Distribution of the distance from the head to the preferred position (histograms). Distribution expected if points were distributed uniformly in panel A are shown in gray (H_0). P-values are computed based on Kolmogorov-Smirnov test.

C: Distribution of the egocentric bearing to the preferred position. B, R, F, L refer to preferred position occurring behind, right, in front or left of the head. P-values are computed based on circular Rayleigh test for uniformity.

bioRxiv preprint doi: https://doi.org/10.1101/684464; this version posted June 27, 2019. The copyright holder for this preprint (which was not certified by peer review) is the author/funder. All rights reserved. No reuse allowed without permission.

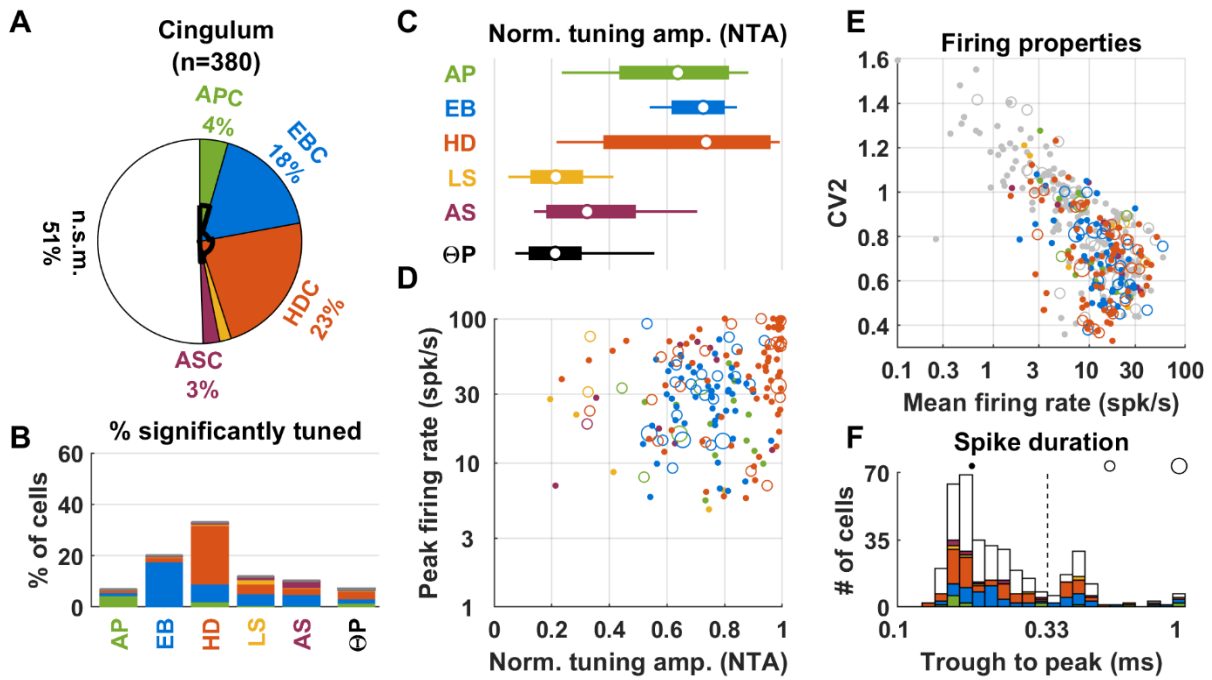

Figure 7 Supplemental 3: Population response in the cingulum. Same legend as in **Fig. 6**.

We implanted and recorded units in the cingulum of seven animals (**Fig. 7S4**). Two animals exhibited minimal locomotor behavior in the arena and were excluded from the population analysis since criteria for coverage of the arena interior were never met (H62M and H65M; responses shown in **Fig. 7S4**). Responses from the remaining 5 animals are shown here.

Neuronal responses: The prominent group of neurons in ATN is HDC, which amount to about half of the population, whereas EBC amount to about half of the RSC population. Accordingly, we expected to encounter large fractions of HDC and EBC in the cingulum. In agreement with this hypothesis, 23% of cells were classified as HDC (A,B) and 18% as EBC (A,B). A detailed description of these response types follows.

Head direction cells: HDC in the cingulum were highly responsive: the median NTA was 0.92 (C), similar (Wilcoxon rank sum test, p=0.16) to the median value in ATN (0.89), and the range of NTA (0.57-0.99 1st-9th decile) overlapped the range in ATN. Although cingulum HDC had identical NTA as ATN HDC, neurons with low firing rate (e.g. ~3 spk/s or less) or low peak responses (e.g. ~10 spk/s or less) were under-represented (compare **Fig. 6D,E** and panels D,E here) and, as a consequence, both mean firing and peak firing of HDC were significantly higher in the cingulum (mean firing: median = 14 vs 9 spk/s, p=2.10^{-3}, Wilcoxon rank sum test; peak firing: median = 48 vs 20 spk/s, p<10^{-5}).

Egocentric boundary cells: The normalized response amplitude of EBC recoded in the cingulum ranged from 0.57 to 0.84 (1st-9th decile) (**C**), overlapping the distribution in the RSC, and with a similar median value (0.75) as in RSC (p=0.7). Furthermore, 39% of cingulum EBC were also significantly tuned to HD (B), in agreements with findings in the RSC (**Fig. 7B**). The median normalized amplitude of these HD

bioRxiv preprint doi: https://doi.org/10.1101/684464; this version posted June 27, 2019. The copyright holder for this preprint (which was not certified by peer review) is the author/funder. All rights reserved. No reuse allowed without permission.

responses was 0.24, similar to the corresponding value in RSC (0.27, p=0.4, Wilcoxon rank sum test). Thus, cingulum and RSC EBC were similar based on normalized response properties. However, cingulum EBC had larger firing rate (14 vs 8 spk/s, $p<2.10^{-3}$) and peak firing (30 vs 16 spk/s, $p<10^{-4}$) (compare **Fig. 7D,E** and panels D,E here).

Other response types: Small fractions of APC, LSC and ASC were encountered in the cingulum (A,B). The median amplitude of APC responses was 0.76, similar to the ATN and other regions (e.g. hippocampus, see below). The NTA of LS responses had a median of 0.33, but was broadly distributed and could reach high values (1st-9th decile: 0.21-0.79). AS responses had large amplitudes (median 0.64, range 0.27-0.87).

Theta rhythm: Only a marginal theta rhythm could be identified in the LFP recorded in cingulum (**Fig. 7S4**). Accordingly, only a small fraction (7%) of neurons exhibited a significant ΘP modulation, and the amplitude of this modulation was very low (median: 0.21).

Firing properties: The average firing rate and CV2 of neurons in the cingulum were inversely correlated (E, Spearman rank correlation=-0.64, $p<10^{-10}$). Average firing rate ranged from 2.5 to 29 spk/s (1st-9th decile; median= 11.7 spk/s) and CV2 from 0.5 to 1.09 (1st-9th decile; median= 0.79), largely overlapped the distribution recorded in ATN and RSC. As expected, the majority of neurons (300/380, 79%) had short-duration spikes (F).

Conclusion: Population responses in the cingulum were highly consistent across all recorded animals (**Fig. 7S4**), confirming that tetrode recordings in the cingulum are possible. The population responses in the cingulum resembled a mixture of ATN and RSC neurons, consistent with anatomical studies that show that it conveys anterior thalamic and RSC projections (Bubb et al. 2018).

bioRxiv preprint doi: https://doi.org/10.1101/684464; this version posted June 27, 2019. The copyright holder for this preprint (which was not certified by peer review) is the author/funder. All rights reserved. No reuse allowed without permission.

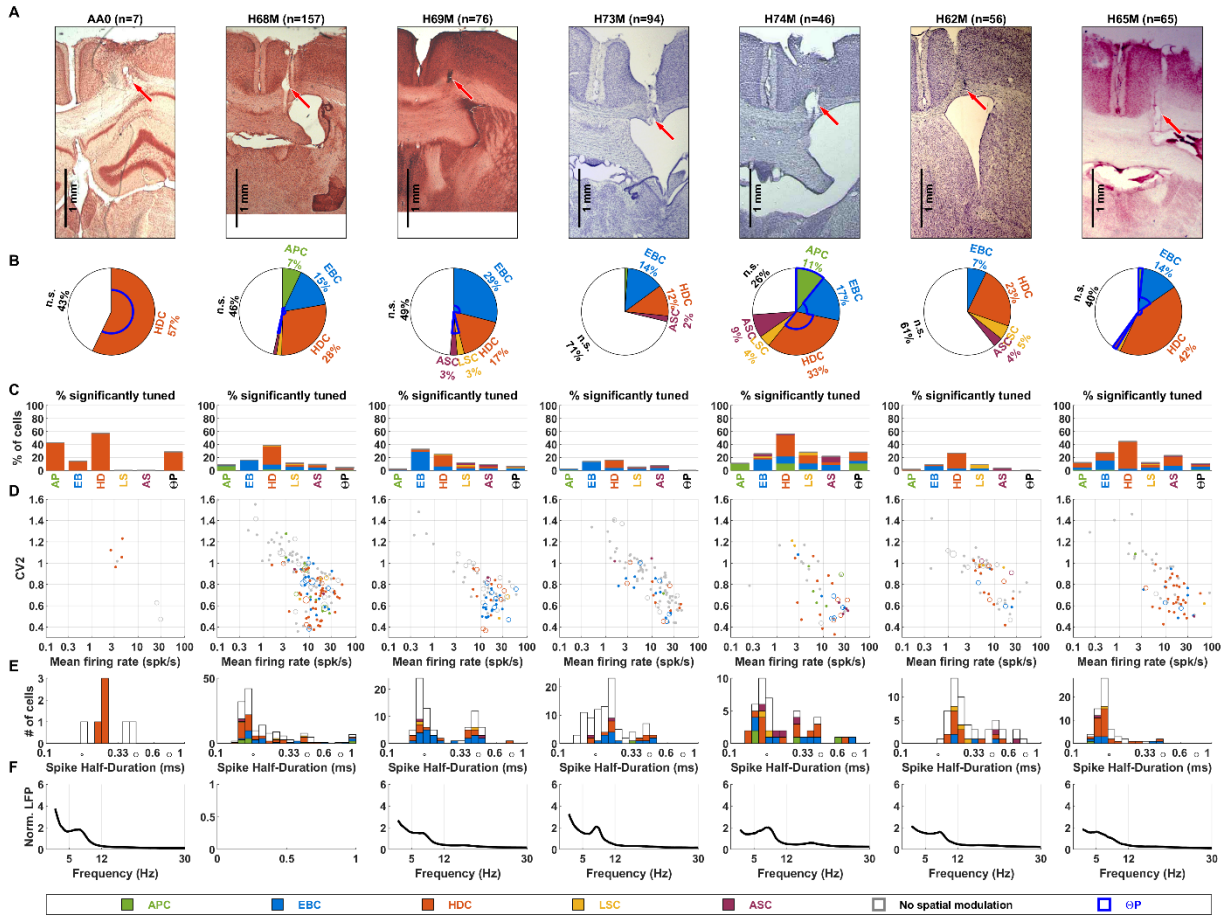

Figure 7 Supplemental 4: Recordings in the cingulum of individual mice. Same legend as in **Fig. 6 Suppl. 1**. Animals H62M and H65M exhibited minimal locomotor behavior and were excluded from the population analysis since criteria for coverage of the arena interior were never met. For reference, we analyzed and displayed neuronal responses based on partially covered arena. We found that population responses were similar as in other animals. This confirms that consistent responses could be recorded in the cingulum of 7 animals and indicates that the LN analysis is robust to partial arena coverage.

bioRxiv preprint doi: https://doi.org/10.1101/684464; this version posted June 27, 2019. The copyright holder for this preprint (which was not certified by peer review) is the author/funder. All rights reserved. No reuse allowed without permission.

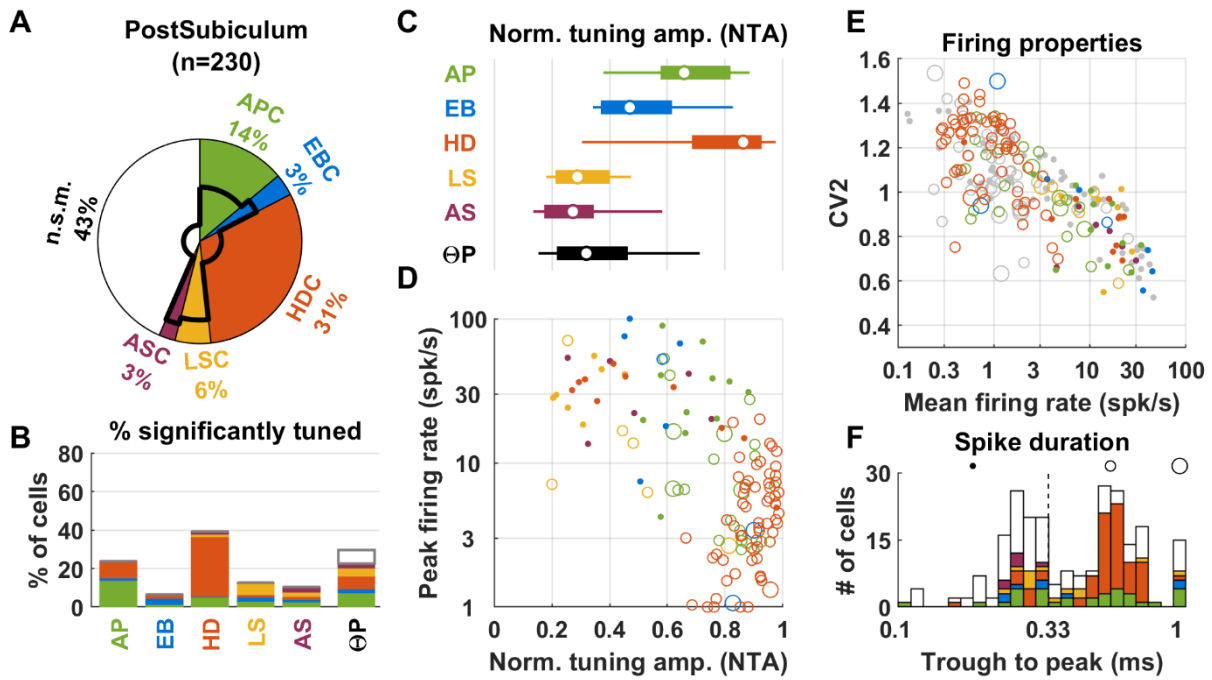

Figure 7 Supplemental 5: Population responses in the Postsubiculum from previously published data (Peyrache et al. 2015). Same legend as in Fig. 6.

We analyzed previously published neuronal responses recorded in the Postsubiculum (Peyrache et al. 2015; 3 animals, 230 neurons). The most prominent cell type were HDC, that amounted to 31% of the population (panel A,B). Most (61/71; 86%) HDC had long spike duration (panel F). These cells, that appear as large open orange symbols in panel D, had large NTA (median = 0.91; 1st-9th decile: 0.77-0.97) and low peak firing (median = 3.8 spk/s; 1st-9th decile: 1.2-10.5 spk/s). These cells likely correspond to layer 3 pyramidal neurons identified as the main population of postsubicular HDC in (Tukker et al. 2015, Preston-Ferrer et al. 2016, Simonnet et al, 2017; Simonnet et Fricker, 2017).

The second most prominent type of response were APC, which amounted to 14% of the population. Most (32/43, 74%) APC had long-duration spikes, and AP responses had generally large NTA (median = 0.67; 1st-9th decile: 0.38-0.89).

We noted that 12 APC were significantly tuned to HD and 20 HDC were significantly tuned to AP, such that, altogether, ~14% of the population encoded AP and HD conjunctively. Cells that encode these variables conjunctively were also reported by Caccuci et al. (2004), although most of these cells were Θ-modulated. In contrast, the conjunctive cells identified in our analysis of Peyrache et al's (2015) data were rarely (9/32, 28%) Θ-modulated.

bioRxiv preprint doi: https://doi.org/10.1101/684464; this version posted June 27, 2019. The copyright holder for this preprint (which was not certified by peer review) is the author/funder. All rights reserved. No reuse allowed without permission.

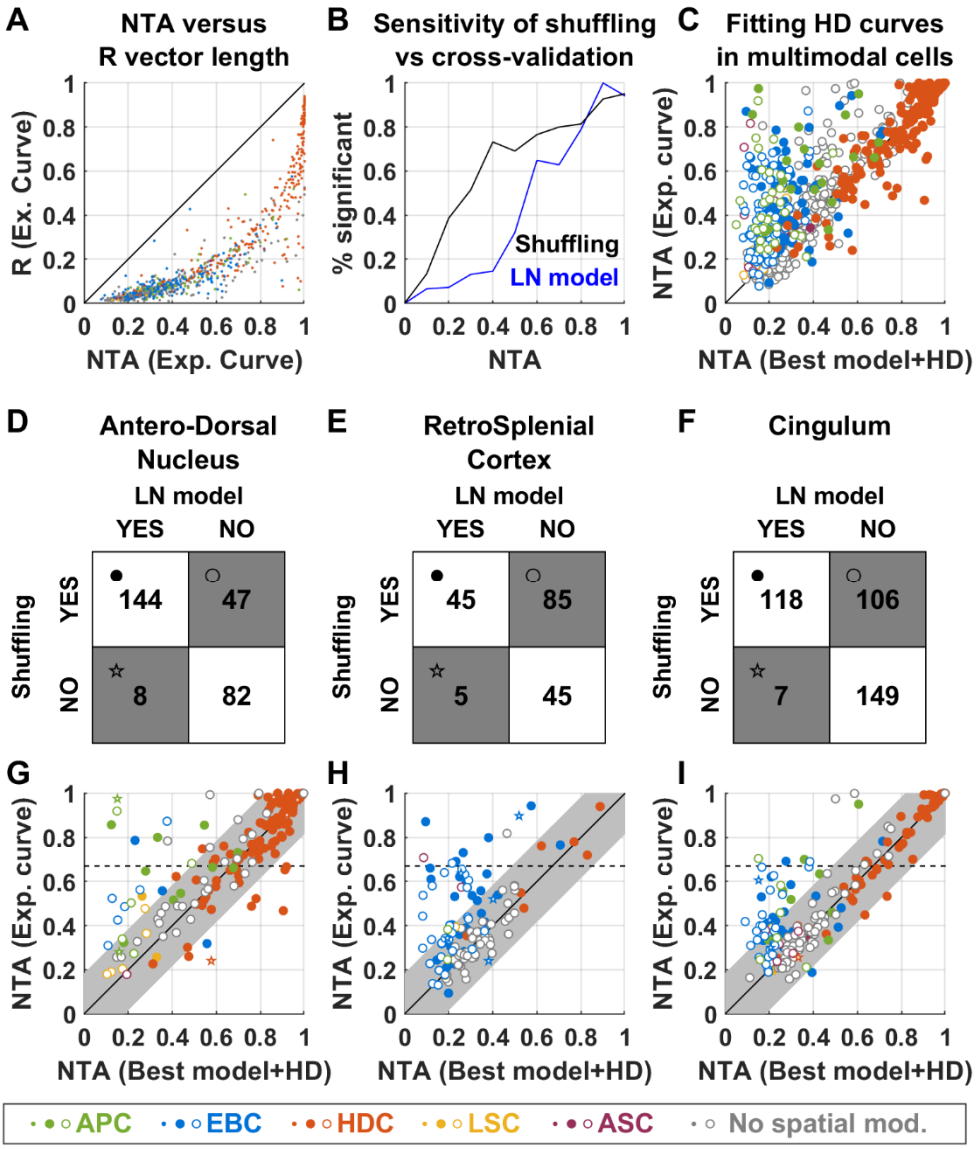

Figure 7 Supplemental 6: Classification of HD cells using the LN model versus traditional approaches.

Here we analyze how the statistical approach used to classify HD cells in the LN model differs from traditional techniques where HD tuning is quantified by the mean vector length |R|, and statistical significance is evaluated by a shuffling test where |R| is considered significant if it is larger than 99% of a set of |R| values produced by randomly shifting the animal's motion relative to the neuronal spike train (Skaggs 1993; Finkelstein et al. 2015). Alternatively, many studies classify cells as HDC when |R| exceeds a threshold, e.g. 0.26 (Jacobs et al. 2017) or 0.4 (Yoder and Taube 2009; Kornienko et al. 2018).

In contrast, the LN model tests for HD tuning by fitting a HD tuning curve to 90% of the recorded data and measuring how the fitted curve accounts for the cell's firing during the remaining 10%. This operation, called cross-validation, is repeated 10 times. A cell is considered HD tuned if the fitting quality is significantly larger than 0 (or than a previous model that doesn't include HD) based on a signed

bioRxiv preprint doi: https://doi.org/10.1101/684464; this version posted June 27, 2019. The copyright holder for this preprint (which was not certified by peer review) is the author/funder. All rights reserved. No reuse allowed without permission.

rank test over these 10 samples. Another fundamental difference between the LN model and traditional approaches is that the LN model fits the cell's firing with multiple variables simultaneously.

Here, we discuss how these differences affect the classification of HD cells by considering data from the ATN, cingulum and RSC only (where most HD-tuned cells are found).

A: Comparison between the traditional measure, |R|, and the NTA measure used in this study. We computed the |R| and NTA values of the experimental tuning curves of all cells (regardless of whether they were significantly tuned to HD). Most data points cluster tightly to form a curve, indicating that there is a close (although non-linear) correspondence between |R| and NTA. Cells are color-coded based on the classification by the LN model (see legend).

B: Comparison between the sensitivities of the cross-validation and shuffling tests. We performed a shuffling test on the |R| value of all cells. Independently, we fitted a LN model where only HD was included. Next, we computed the percentage of cells that are classified as HD-tuned based on a shuffling test (black curve) or the LN model (blue curve) as a function of NTA. As expected, almost all cells pass both tests when the NTA is high (>0.8). In contrast, fewer cells with intermediate NTA (0.2-0.8 range) pass the LN model's cross-validation test, compared to the shuffling test. Note that cells that pass the shuffling test but not the cross-validation test are not 'false positive', since their tuning is indeed significantly based on the shuffling test. Instead, this analysis indicates that the cross-validation procedure is less sensitive than the shuffling test.

C: Previous studies (Muller et al. 1994; Cacucci et al. 2004; Rubin et al. 2014) have pointed out that responses to variables other than HD (e.g. AP or EB) can be erroneously interpreted as HD tuning. When this happens, HD tuning will appear high when fitting the LN model with only the HD variable, or when computing the experimental tuning curve, but will be lower when the response to other modalities is accounted for, as done by the LN model in general. To appreciate this, we plot the NTA of the experimental HD tuning curve versus the NTA of the HD curve fitted by the LN model. The latter was computed based on the cell's best model (for HD-tuned cells) or based or by adding the HD variable to the best model. Filled/open symbols represent cells that are HD tuned/not tuned based on the full LN model. Cells are color-coded based on the classification by the LN model (see legend). Many AP and EB cells (green and blue) appear above the diagonal, indicating that responses that can be accounted for by the AP or EB models are erroneously interpreted as HD tuning when considering only the HD model. This overestimation may happen in cells that are really HD tuned (closed symbols) or not (open symbols).

From B and C, we conclude that (1) the shuffling test is more sensitive than the cross-validation procedure, and that (2) computing NTA (or equivalently |R|) from experimental tuning curves is prone to overestimating HD tuning in multimodal cells. Next, we examine how these approaches differ, in practice, when applied to ATN, RSC and cingulum.

D-F: Contingency matrices indicating the number of cells classified as HD-tuned or not by the LN model and shuffling method in ATN (D), RSC (E) and cingulum (F). The symbols shown in the matrix correspond to the symbol code in panels G-I. We find that these methods generally agree in the ATN: 144 cells are classified as HD-tuned and 82 as HD non-tuned by both, i.e. the classification match in 226/281 (80%)

bioRxiv preprint doi: https://doi.org/10.1101/684464; this version posted June 27, 2019. The copyright holder for this preprint (which was not certified by peer review) is the author/funder. All rights reserved. No reuse allowed without permission.

cells. 47 cells (17% of ATN) are classified as HD-tuned by only the shuffling method, and a negligible fraction by only the LN model. The two classifications diverge to a larger extent in RSC and cingulum, where 48% and 27% of cells are classified as HD-tuned based on the shuffling methods only.

G-I: To elucidate the origin of these discrepancies, we plot the NTA of the experimental HD tuning curve versus the curve fitted by the LN model (as in panel C). Cells that are HD-tuned based on both classifications are shown as filled symbols. Cells that are HD-tuned based on the shuffling/cross-validation methods only are shown as open disks/stars. Cells are color-coded based on the classification by the LN model (see legend).

A sizeable fraction of cells are classified as HD tuned based on the shuffling method only (open symbols, n=237 across all 3 areas), and we reason that this may occur for two reasons: (1) because the NTA of some cells is overestimated when computing the experimental curve (see panel C), in which case cells will appear above the diagonal and/or (2) because the shuffling test is more sensitive for cells with low NTA (see panel B). To quantify approximatively how many cells fall in these two categories, we estimate a confidence interval around the diagonal by considering cells that are classified as HDC by both methods (solid red). The confidence interval width is set at the 95% percentile of the distance distribution of these cells from the diagonal (0.13). We find that 185/237 (78%) of open symbols fall within this interval. These likely correspond to cells where HD tuning was likely *not* over-estimated, and that were classified as HD-tuned because of the shuffling test's larger sensitivity. These cells are likely genuinely HD-tuned, although with a low amplitude. In contrast, HD tuning may have been overestimated in cells that appear above the interval (52/237; 22% of open symbols), and the classification as HD-tuned may be erroneous. In total, this category of potentially mis-classified cells represents 15/281 (5%) ATN cells, 18/180 (10%) RSC cells and 19/380 (5%) cingulum cells.

Finally, we note that some studies require HD cells to pass a threshold, i.e. $|R|>=0.26$ in (Jacobs et al. 2017) or $|R|>=0.4$ (Yoder et al. 2009; Kornienko et al. 2018). Based on panel A, we estimate that $|R|>0.26$ corresponds to NTA>=0.67 (broken lines in G-I). When this threshold is added to the shuffling test, a total of 220 cells are classified as HD-tuned, out of which 190 (87%) are also classified as HD-tuned by the LN model. However, this test now rules out 137 out of 327 cells (42%) that are classified as HD-tuned by the LN model, including, in particular, most (76/91, 84%) cells identified as APC or EBC with significant HD tuning by the LN model. Thus, using a threshold allows selecting well-tuned HD cells in a conservative manner, but tends to miss weaker HD cells and multimodal cells.

bioRxiv preprint doi: https://doi.org/10.1101/684464; this version posted June 27, 2019. The copyright holder for this preprint (which was not certified by peer review) is the author/funder. All rights reserved. No reuse allowed without permission.

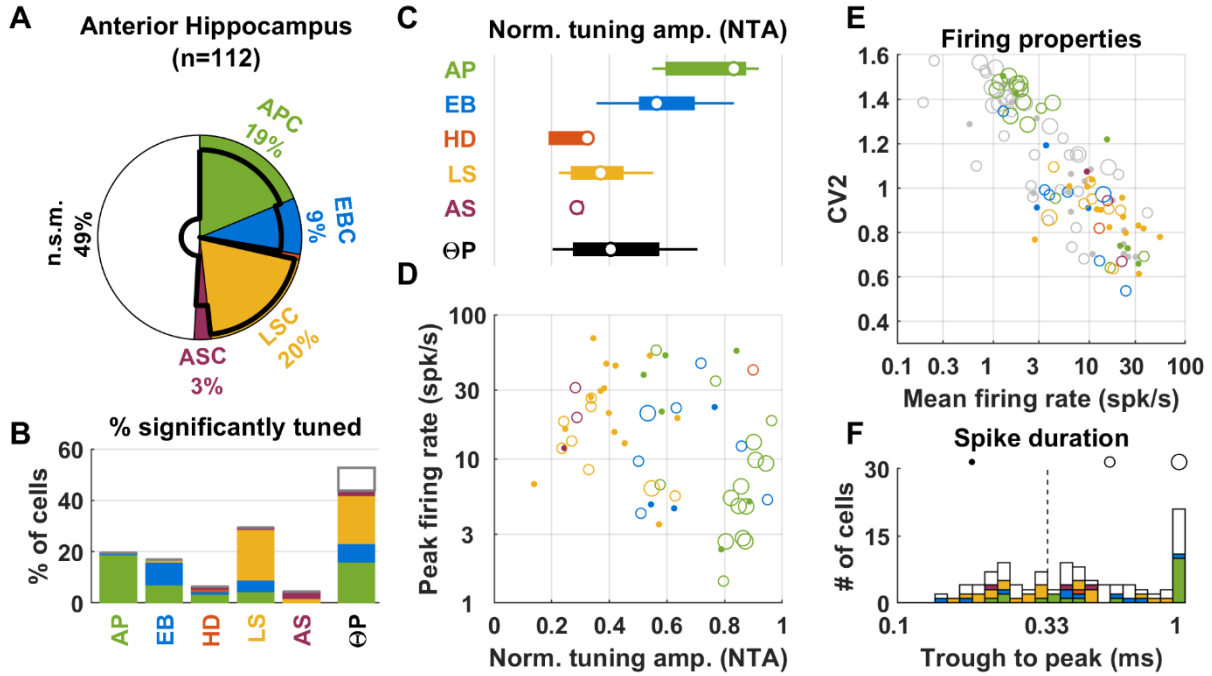

Figure 8: Population responses in the hippocampus. Same legend as in **Fig. 6**.

bioRxiv preprint doi: https://doi.org/10.1101/684464; this version posted June 27, 2019. The copyright holder for this preprint (which was not certified by peer review) is the author/funder. All rights reserved. No reuse allowed without permission.

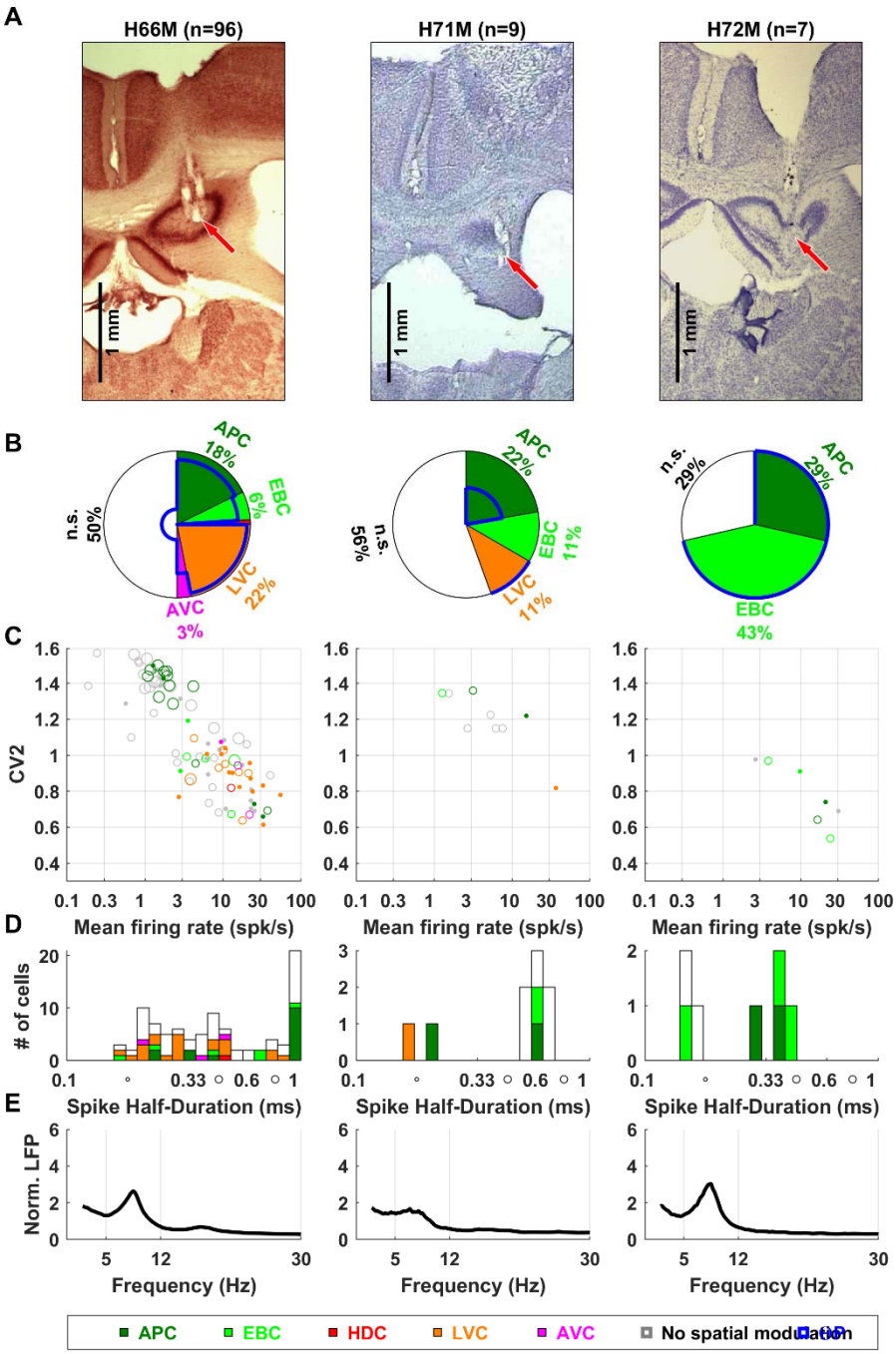

Figure 8 Supplemental 1: Recordings in the hippocampus of individual mice. Same legend as in **Fig. 6 Suppl. 1.**

bioRxiv preprint doi: https://doi.org/10.1101/684464; this version posted June 27, 2019. The copyright holder for this preprint (which was not certified by peer review) is the author/funder. All rights reserved. No reuse allowed without permission.

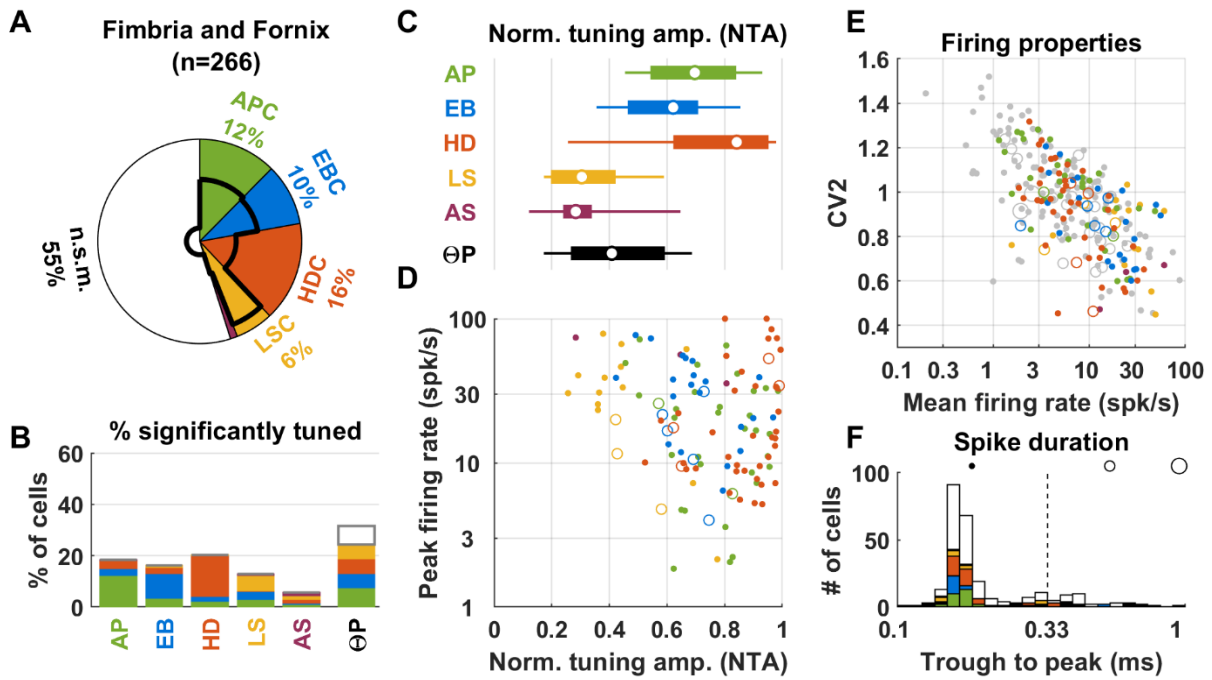

Figure 8 Supplemental 2: Population responses in the fimbria and fornix. Same legend as in **Fig. 6**. A summary of population responses follows.

APC: A fraction (12%) of cells recorded in the fimbria and fornix were classified as APC (panels A,B). APC in the fimbria exhibited large NTA (panels C,D, median = 0.8, 1st-9th decile: 0.56-0.95); as well as large peak firing rate (median 17 spk/s, 1st-9th decile 3-48 spk/s; D).

HDC: A fraction (16%) of cells recorded in the fimbria and fornix were HDC (panels A,B). The median NTA was high (panels C,D; median: 0.91, 1st-9th decile 0.65-0.98) and similar as in ATN and cingulum (p=0.49 and p=0.62 respectively). The median peak firing rate (15 spk/s; 1st-9th decile: 7-73) was similar to the value observed in the ATN (p=0.36) but lower than in the cingulum ($p<10^{-4}$).

Other cells: We also encountered a sizeable fraction of EBC (9%, panel A) that had large NTA (median 0.7, range 0.52-0.9), similar to hippocampus (p=0.24); as well as a fraction of LSC (6%, Fig. 10C) with moderate NTA (median 0.43, 1st-9th decile: 0.29-0.69) similar to hippocampal LSC (p=0.15).

Theta rhythm: Across the entire population of recorded neurons, 32% of fimbria neurons were ΘP modulated. However, this fraction increased to 54% when only spatially modulated neurons were considered.

Spiking properties: Mean firing rate and CV2 were inversely correlated, as in other regions (panel E, Spearman rank correlation=-0.65, $p<10^{-10}$). Most cells (86%) had short duration spikes, as expected from recordings performed in the white matter.

bioRxiv preprint doi: https://doi.org/10.1101/684464; this version posted June 27, 2019. The copyright holder for this preprint (which was not certified by peer review) is the author/funder. All rights reserved. No reuse allowed without permission.

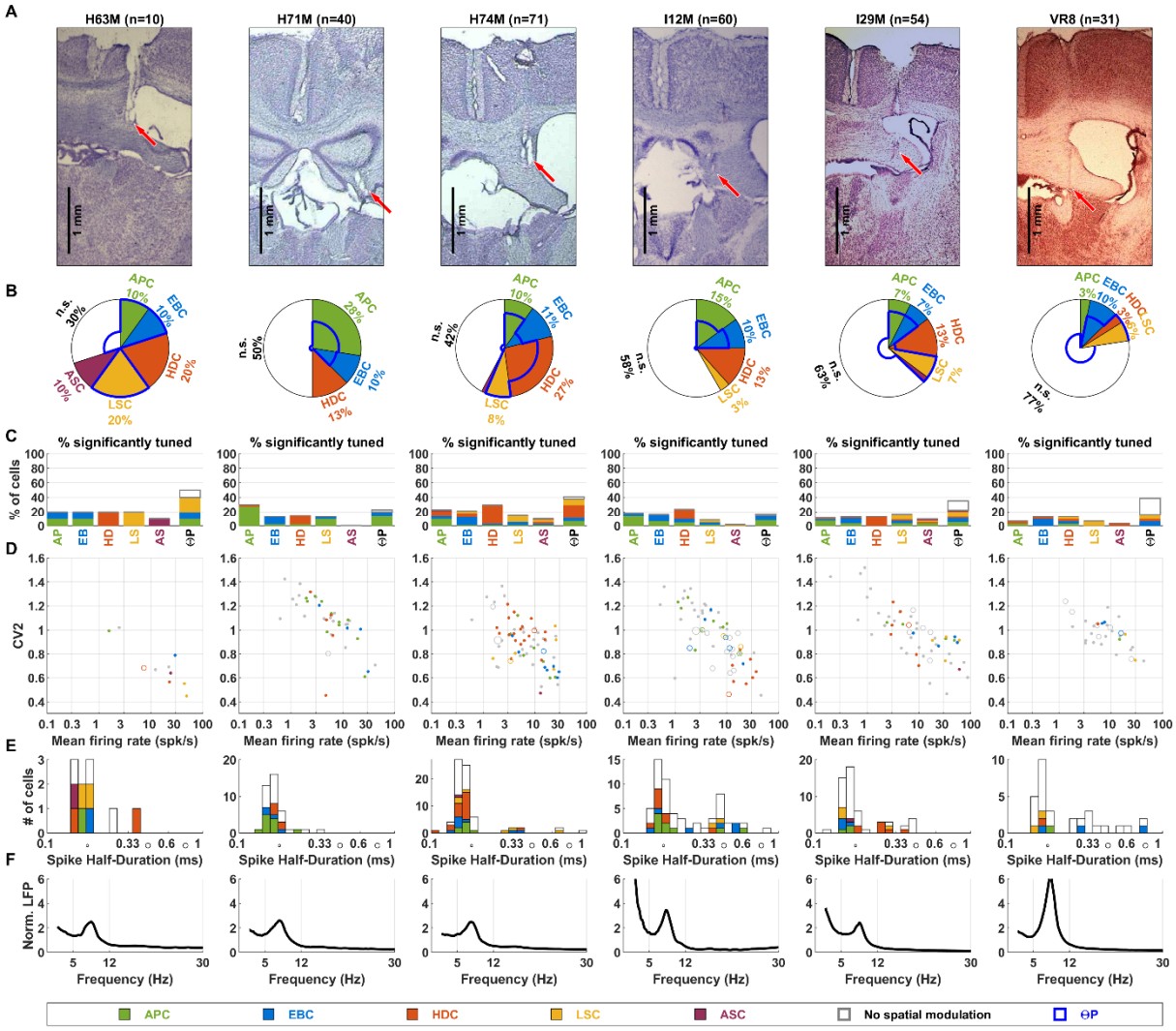

Figure 8 Supplemental 3: Recordings in the fimbria and fornix of individual mice. Same legend as in **Fig. 6 Suppl. 1.**

bioRxiv preprint doi: https://doi.org/10.1101/684464; this version posted June 27, 2019. The copyright holder for this preprint (which was not certified by peer review) is the author/funder. All rights reserved. No reuse allowed without permission.

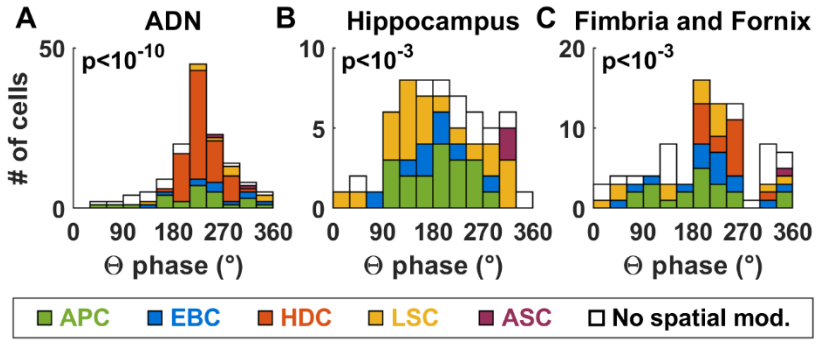

Figure 8 Supplemental 4: Distribution of preferred phase of ΘP-modulated cells. Distributions are shown as histograms, where phases of 0, 90, 180 and 270° correspond to the trough, ascending phase, crest and descending phase of the LFP. Cells are color-coded based on their classification.

About half of ATN and hippocampal cells, and half of spatially-modulated neurons recorded in the fimbria, responded preferentially at a certain phase of the Θ-band LFP. We found that the distribution of preferred phase were non-uniform. In ATN (**A**), most cells responded preferentially during the descending phase (180-360°), with an average preferred phase of 230±10°. In particular, the two main classes of ΘP-modulated ATN neurons, HDC and APC, had an identical average preferred phase (230 vs 235°, p=0.7, Watson-Williams test). In the hippocampus (**B**), the average preferred phase was 193±29° amongst APC, whereas preferred phases were distributed uniformly amongst LSC (yellow). In the fimbria (**C**), HDC responded preferentially in the descending phase (238±20°) whereas APC fired closer to the LFP crest 184±40° ($p=5.10^{-4}$ versus ATN, Watson-Williams test).

bioRxiv preprint doi: https://doi.org/10.1101/684464; this version posted June 27, 2019. The copyright holder for this preprint (which was not certified by peer review) is the author/funder. All rights reserved. No reuse allowed without permission.

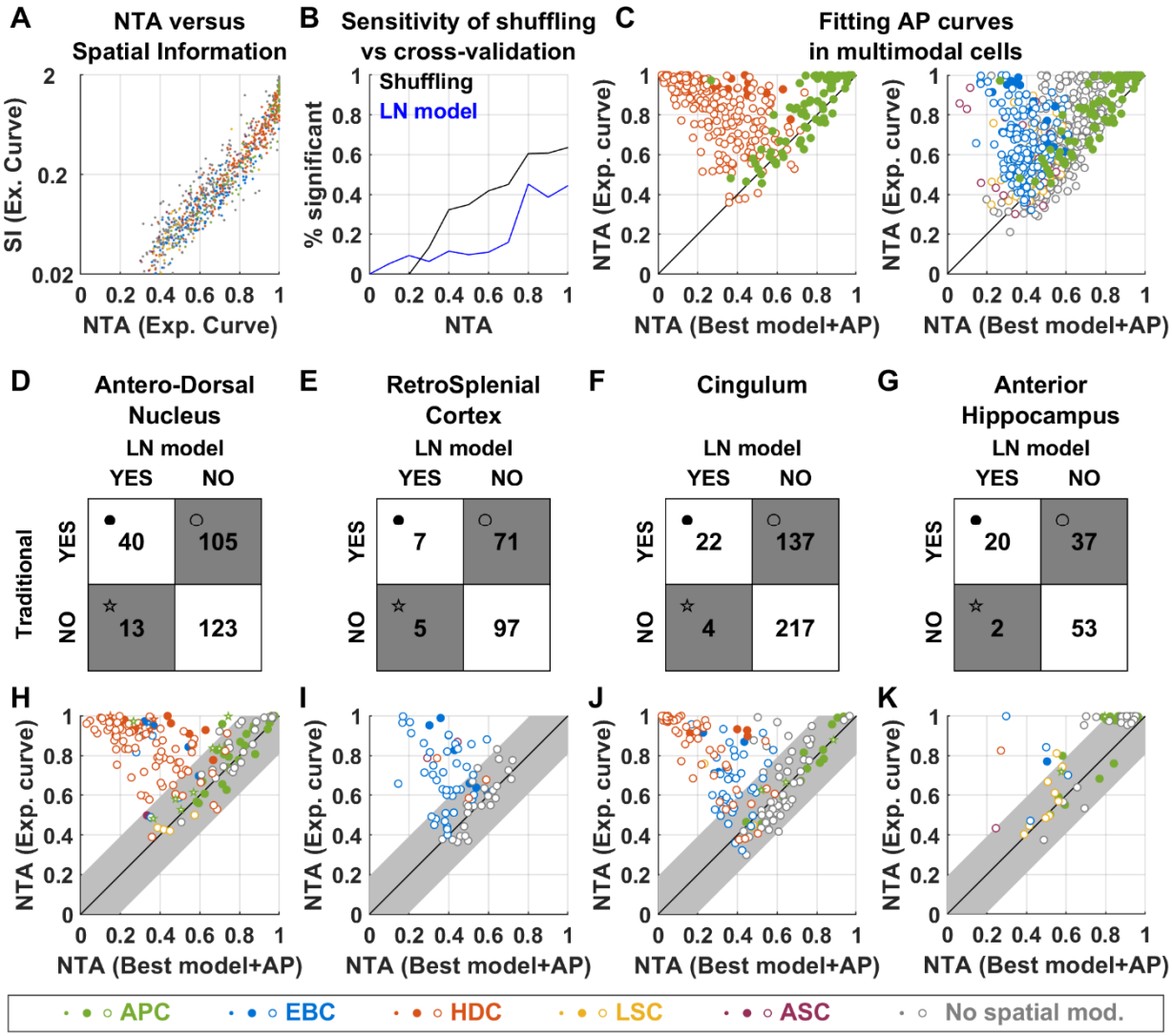

Figure 8 Supplemental 5: Classification of AP cells using the LN model versus traditional approaches.

We now follow the same logic as in **Fig. 8 S2** to analyze how the statistical approach used to classify AP cells in the LN model differs from traditional techniques, where AP tuning is quantified by spatial information (SI) of the tuning curve, and where a give SI value is considered significant if it is larger than 99% of a set of shuffled values (Skaggs 1993; Rubin et al. 2014). We consider data from the ATN, cingulum and anterior hippocampus only (where most AP-tuned cells are found).

A: Comparison between spatial information (SI), and the NTA measure used in this study. We plot the SI and NTA of the experimental tuning curves of all cells (regardless of whether they were significantly tuned to AP). Most data points cluster tightly to form a curve, indicating that there is a close correspondence between SI and NTA. Cells are color-coded based on the classification by the LN model (see legend).

bioRxiv preprint doi: https://doi.org/10.1101/684464; this version posted June 27, 2019. The copyright holder for this preprint (which was not certified by peer review) is the author/funder. All rights reserved. No reuse allowed without permission.

B: Comparison between the sensitivities of the cross-validation and shuffling tests, as in **Fig. 8 S2B**. We find that, even when the NTA is high (>0.8), only ~50% cells pass the tests. This indicates that even an apparent high AP tuning may not be significant, in contrast with HD tuning (**Fig. 8 S2B**). This difference may be due to the fact that repetitively covering the 2D surface of the arena, which is required to archive statistical robustness, is harder than covering the 1D space of head direction. Similar to HD tuning, we find that the cross-validation procedure is generally less sensitive than the shuffling test for intermediate NTA.

C: In multimodal cells, responses to variables other than AP (e.g. HD) can be erroneously interpreted as AP tuning. We plot the NTA of the experimental AP curve versus the NTA of the AP curve fitted by the LN model. For readability, we separate this panel in two plots, with HD cells and AP cells on the left and AP cells and other cell types on the left. Filled/open symbols represent cells that are HD tuned/not tuned based on the full LN model. Cells are color-coded based on the classification by the LN model (see legend). We find a striking number of HD cells (red) converging towards the upper left corner, i.e. where AP tuning appears very strong if HD tuning is not accounted for first. Thus, as pointed out by previous studies (Peyrache et al. 2017), HD cells may easily be confounded for AP cells. We also find that AP tuning is often overestimated in EB cells (blue).

D-G: Contingency matrices indicating the number of cells classified as AP-tuned or not by the LN model and shuffling method in ATN (D), RSC (E), cingulum (F) and anterior hippocampus (G). We first note that most cells that were classified as AP-tuned by the LN model are also classified as AP-tuned by the shuffling test (ATN: 40/53, i.e. 75%; cingulum: 22/26, i.e. 85%; hippocampus: 20/22, i.e. 91%). This validates our finding that the ATN and cingulum contain APC populations. Next, we observe that the ATN, RSC and cingulum contain large fractions of cells (37%, 39% and 36% respectively) of cells that are classified as AP-tuned by the shuffling test only (open circles).

H-K: As in **Fig. 8 S2G-I**, we plot the NTA of the experimental AP curve versus the curve fitted by the LN model. Cells that were tuned based on both classifications are shown as filled symbols. Cells that are tuned based on the shuffling/cross-validation methods only are shown as open disks/stars. Cells are color-coded based on the classification by the LN model (see legend). We draw a confidence interval, with a width estimated at 0.14 (based on cells classified as APC by both methods) around the diagonal.

In the ATN (panel H), 67 cells are classified as AP tuned based on the shuffling procedure only and positioned above the confidence interval. Most of these cells (63/67) are HD cells (open orange circles). In these cells, AP tuning is vastly overestimated, and the classified as AP-tuned by the shuffling procedure is clearly incorrect. This group amounts to 63/135 HDC, i.e. 47% of ATN HD cells. In the RSC (panel I), we also find a large group cells above the confidence interval, most of which (26/29) are EBC (open blue symbols). This group amounts to 26/81 EBC, i.e. 32% of RSC EBC. We also find a sizeable group of open symbols within the confidence interval (42 cells, i.e. 59% of cells classified as AP based on the shuffling method only). This suggests that a population of cells with weak but significant AP tuning, that would not have been detected by the LN model, may exist in the RSC. In the cingulum (panel J), we find both HDC and EBC above the diagonal, amounting to 45% of HDC and 40% of EBC; as well as a group of cells within the confidence interval (47% of cells classified as AP based on the shuffling method only).

bioRxiv preprint doi: https://doi.org/10.1101/684464; this version posted June 27, 2019. The copyright holder for this preprint (which was not certified by peer review) is the author/funder. All rights reserved. No reuse allowed without permission.

These results are in line with the hypothesis that cingulum carries a mixture of ATN and RSC signals. In total, 67/281 (24%) ATN cells, 29/137 (16%) RSC cells and 72/380 (19%) cingulum cells, placed above the diagonal, were incorrectly classified as AP-tuned by the shuffling test.

In the hippocampus (panel K), most (30/37) open symbols falls within the confidence interval. Furthermore, many cells cluster at the upper right corner of the graph, indicating that they are highly tuned to AP even when this tuning is overestimated by the experimental curve. This indicates that most cells identified by the shuffling test may be genuine AP cells, and that the LN model may have lacked the sensitivity to identify them. A possible remedy for this lack of sensitivity could be to perform longer recording sessions.

bioRxiv preprint doi: https://doi.org/10.1101/684464; this version posted June 27, 2019. The copyright holder for this preprint (which was not certified by peer review) is the author/funder. All rights reserved. No reuse allowed without permission.

Suppl. Movie 1: Response of a RSC EBC (same as in Fig. 5) during free exploration. The movie shows the animal's motion and neuronal activity recorded during two minutes of free exploration. **Upper left panel**: animal motion from an allocentric point of view. The arena's boundary is shown in white, with the cue card represented as a dark gray arc. As time elapses, the animal's trajectory (light blue) and neuronal spikes (red dots) are shown. The arrow indicates the position of the nearest wall. The **right panel** displays exactly the same image, except for the light blue trajectory and red dots. The image is rotated in order to appear in egocentric coordinates. The light blue trajectory and red dots now represent the trajectory of the nearest boundary in egocentric coordinates. Spikes concentrate in front of the head, indicating that the neuron responds when the head is close to the wall and faces it. Lower left panel: raw neuronal data.